Simulation of impacts between spherical rigid bodies with frictional effects

Eliana Sánchez[1], Alejandro Cosimo[1], Oliver Brüls[2], Alberto Cardona[1] and Federico J. Cavalieri[1]

[1]Centro de Investigación de Métodos Computacionales (CIMEC), Colectora Ruta Nac. Nro. 168, Km 0, Paraje El Pozo, 3000 Santa Fe, Argentina.

[2]University of Liège, Department of Aerospace and Mechanical Engineering, Allée de la Découverte 9, 4000 Liège, Belgium.

Abstract

This work studies the impact between spherical rigid bodies in the frame of nonsmooth contact dynamics considering friction effects. A new impact element formulation based on the classical instantaneous local Newton impact law is presented. The kinematics properties of the spheres are described by a rigid body formulation with translational and rotational degrees of freedom referred to an inertial frame. In addition, an extension of the nonsmooth generalized-α time integration scheme applied to collisions with multiple impacts including Coulomb's friction law is given. Six numerical examples are presented to evaluate the robustness and the performance of the proposed methodology.

1 Introduction

The simulation of impacts between spherical rigid bodies under friction is a challenging research topic. Roughly speaking, in these problems, two scenarios can arise: (i) **single impacts**, when two bodies are in contact at a single point and the impact occurs at this point, and (ii) **multiple impacts** when there are several bodies are in contact in various points and the impacts occur simultaneously in some of them [51].

From a numerical perspective, the literature contains many works oriented to solving the impact using a continuous contact force model based on Hertz's law and a hysteresis damping force to introduce energy dissipation during the contact process [66, 38, 41, 36, 26, 67]. A complete review of several contact forces can be found in Rodrigues da Silva *et al* [56]. These models assume that the impact time duration is very small but of finite duration. They have the disadvantage of requiring a large amount of computational time due to the use of very small time steps to accurately capture the behavior of the bodies. Moreover, penetration between the bodies is unavoidable in this kind of approach. To overcome the limitations of these continuous contact models, some authors proposed other schemes that can solve efficiently problems involving strong discontinuities. Jean Jacques Moreau [47], proposed a general framework for nonsmooth modeling of rigid body dynamics. Other authors as Pfeiffer and Glocker, discussed impacts and friction in multi–body systems [54] and a wide overview of non–smooth dynamics is presented by Brogliato in [10]. Nonsmooth time integration based on event-driven schemes can be found in the following references [59, 1, 2, 57]. Then, Brüls and colaborators proposed a nonsmooth generalized-α time integrator scheme which overcomes many problems of the Moreau-type time-stepping schemes, see [17, 12, 13]. More recently, Capobianco *et al* [14] proposed a nonsmooth generalized-α method for the simulation of mechanical systems with frictional contact where unlike to the previous references, the constraints are satisfied on acceleration level. Tasora and Anitescu [61] and Huang *et al* [37] address the problem of impact of spherical rigid bodies by modelling rolling friction with a second-order cone complementarity problem. In this research direction, Acary and Bourrier [3] presented a formulation of contact between spheres and between a sphere and a plane, considering the Coulomb friction's law with rolling resistance as a cone complementary problem based on the work of De Saxcé and Feng [24, 23]. Recently, Sánchez *et al* [60] analyzed the general motion of a sphere in contact with a rigid planar surface with rolling, sliding and spinning friction in the context of nonsmooth contact dynamics.

In the case of multiple impacts, a wide variety of contact models has been proposed by extending single-impact formulations. The approach of Darboux-Keller [22] includes contact compliance by introducing a distributing rule, and it considers plastic deformation through the bi-stiffness contact model along with energetic coefficients of restitution. Later, Liu and Brogliato extended this methodology to study multi-impact collisions related in granular chain problems [45, 46]. Another alternative is by using the classical Poisson impact law [55, 33] or the Hurmuzlu's ICR Law which was applied to solve various types of systems like chains of aligned balls [29] and the rocking problem [21], among others. Other approaches are based on spring-dashpot models [16, 38, 40, 63]. Again, the main drawback of this methodology is the large computation time required for the simulation because of the adoption of very small time steps.

When impact time duration is considered instantaneous, the impact process is modeled by a function, which can be explicitly or implicitly defined, relating the post- and the pre-impact velocities. The Newton model belongs to this group; unlike the Poisson model, the coefficient of restitution relates the pre- and post- impact velocities [50]. Moreau formulated the impact by a differential inclusion; thus, it can be adapted in a relatively easy way to perform computational numerical simulations in nonsmooth dynamics [47]. However, in case of multiple impacts, the admissible solutions are restricted to few cases and they may be far from the experimental observations [31]. Other alternatives can be found in [27, 10, 35] where the strength and weakness of each model is discussed in [51].

Recently, Cosimo *et al* [19] presented a general methodology to simulate multiple impact collisions assuming instantaneous impacts times and considering simultaneity of impacts and propagation effects without compliance of the system in the framework of the nonsmooth generalized-α time integrator scheme. The method is a time stepping scheme which does not require any synchronisation of the time steps with the impacts events and can deal with a large number of impacts. Additional complications arise when impact problems involve friction effects, because another non-linearity has to be included in the formulation to consider the friction effects. Several references can be found in the literature about the treatment of Coulomb's friction in the frame of Moreau's law [48, 49, 58]. The LBZ model with friction is given in [64, 65, 11], meanwhile friction models with Newton and Poisson laws can be found in [9, 25, 44, 30] and [32, 42, 52, 53, 54], respectively.

In this work, a new formulation for frictional contact and impact between two rigid spherical bodies is presented. The motion of each body is directly referred to an inertial frame for the kinematic description with large rotations and displacements, as proposed by Géradin and Cardona [34]. The time integration scheme for the equations of motion corresponds to the version of the nonsmooth generalised-α integrator presented in [20]. Because of the rigid body assumption, deformations and stresses at the contact zone are neglected. Then, the change in velocity is instantaneous and determined by the restitution coefficient, which depends on the contact surface characteristics of the contacting bodies. This coefficient is obtained experimentally and classified in tables. Then, the Coulomb's friction law is used for the frictional case, and the value of the frictional forces is determined by a single friction coefficient which is obtained experimentally. More complex models can be found in the literature; however, the Coulomb friction model is widely accepted, as evidenced by the bibliography presented in this work. No other dissipative effects have been taken into account in the numerical examples presented. These hypotheses are of widespread use, and they are enough to accurately capture the global behavior of mechanical systems as those presented in the examples of this work, with solutions which are very close to experimental observations.

A new formulation for the modelling of frictional contact with impacts between two rigid spherical bodies is presented by Sánchez *et al.* [60] where the frictional contact between a sphere and a rigid plane is studied. Similar to the formulation of Sánchez *et al.*, the contact/impact problem between two rigid spherical bodies is solved here using an augmented Lagrangian formulation [4] which was already applied by Gálvez *et al.* [28] to dynamic problems with friction. The main contributions and differences with respect to the work of Sánchez *et al.* are listed below,

- A new formulation of the frictional contact between two spherical rigid bodies in the framework of a nonsmooth technique is presented. The constraints and constraint gradients, both at position and velocity levels, are developed. The analytical expressions for the calculation of the internal force vectors and Hessian matrices are given.

- A simplification of the constraints is introduced in order to reduce the complexity of the implementation. The limitations of the simplifying assumptions are studied.

- An extension of the algorithm to model multiple impacts with friction is presented. The proposal is based on the frictionless multiple impact algorithm presented by Cosimo *et al.* [19]. Here, the algorithm is based on modifying the active set of the velocity correction, defining a sequence of impact problems on a vanishing time interval. Then, the active set of each velocity-level sub-problem is redefined in the normal and in the tangential directions (to consider friction), in such a way that closed contacts with zero pre-impact velocity are considered inactive [19]. New expressions of the internal forces vector at velocity level are developed.

- A numerical comparison of results between the proposed method and the continuous impact method is presented for a test-case involving multiple impacts with friction, showing that the computational time is significantly reduced when using the present methodology.

Six numerical examples are presented to validate and to evaluate the performance of the method. The numerical implementation and simulations presented in this work were carried out in the research finite element code Oofelie, often used for general industrial applications as well as for academic studies. This software allows to simulate non-linear dynamic mechanical systems composed by rigid and flexible components with an efficient framework to deal with finite rotations and to automatically assemble the equations of motion [15].

This work is organized as follows: Section 2 gives a brief explanation of the decoupled version of the nonsmooth generalized-α time integrator. Section 3 describes the frictional contact formulation. Then, the modifications of the active set and of the internal force vector at velocity level to consider collisions with simultaneous multiple impacts and friction are presented. The equations related with the sphere-sphere contact element are developed in Section 4. Finally, Section 5 presents numerical examples which demonstrate the robustness of the proposed algorithm. Final conclusions are drawn in Section 6.

2 Time Integration of Nonsmooth Equations of Motion

The time integration scheme used in this work to solve the equations of motion of a multibody system with unilateral and bilateral constraints, is the decoupled version of the nonsmooth generalized–α described in Cosimo *et al* [20]. This is an implicit time integrator scheme where the final system of equations results in three decoupled sub-problems to be solved at each time step by an iterative Newton semi-smooth method, which can also be interpreted as an active set method. The first sub-problem corresponds to the smooth motion contribution of the system, where the equations of motion are integrated with second order accuracy by means of the generalized–α scheme [20]. The second and third sub-problems compute the impulsive contributions (non smooth) at position and at velocity levels, yielding a first-order accurate solution of the system with impacts. The integrator for a general multibody system that includes unilateral and bilateral constraints is written as follows,

$$\begin{aligned}
\boldsymbol{M}(\breve{\boldsymbol{q}}_{n+1})\dot{\breve{\boldsymbol{v}}}_{n+1} - \boldsymbol{f}(\breve{\boldsymbol{q}}_{n+1}, \breve{\boldsymbol{v}}_{n+1}, t_{n+1}) - \boldsymbol{g}^{\overline{\mathcal{U}},T}_{\breve{\boldsymbol{q}},n+1}\left(k_s \breve{\boldsymbol{\lambda}}^{\overline{\mathcal{U}}}_{n+1} - p_s \boldsymbol{g}^{\overline{\mathcal{U}}}_{\breve{\boldsymbol{q}},n+1}\,\breve{\boldsymbol{v}}_{n+1}\right) &= \boldsymbol{0} && \text{(1a)}\\
-k_s \boldsymbol{g}^{\overline{\mathcal{U}}}_{\breve{\boldsymbol{q}},n+1}\,\breve{\boldsymbol{v}}_{n+1} &= \boldsymbol{0} && \text{(1b)}\\
\boldsymbol{M}(\breve{\boldsymbol{q}}_{n+1})\boldsymbol{U}_{n+1} - \frac{h^2}{2}\boldsymbol{f}^p - \boldsymbol{g}^{\mathcal{A},T}_{\breve{\boldsymbol{q}},n+1}\left(k_p \boldsymbol{\nu}^{\mathcal{A}}_{n+1} - p_p \boldsymbol{g}^{\mathcal{A}}_{n+1}\right) &= \boldsymbol{0} && \text{(1c)}\\
-k_p \boldsymbol{g}^{\mathcal{A}}_{n+1} &= \boldsymbol{0} && \text{(1d)}\\
-\frac{k_p^2}{p_p}\boldsymbol{\nu}^{\overline{\mathcal{A}}}_{n+1} &= \boldsymbol{0} && \text{(1e)}\\
\boldsymbol{M}(\boldsymbol{q}_{n+1})\boldsymbol{W}_{n+1} - h\boldsymbol{f}^v - \boldsymbol{g}^{\mathcal{B},T}_{\breve{\boldsymbol{q}},n+1}\left(k_v \boldsymbol{\Lambda}^{\mathcal{B}}_{n+1} - p_v \mathring{\boldsymbol{g}}^{\mathcal{B}}_{n+1}\right) &= \boldsymbol{0} && \text{(1f)}\\
-k_v \mathring{\boldsymbol{g}}^{\mathcal{B}}_{n+1} &= \boldsymbol{0} && \text{(1g)}\\
-\frac{k_v^2}{p_v}\boldsymbol{\Lambda}^{\overline{\mathcal{B}}}_{n+1} &= \boldsymbol{0} && \text{(1h)}
\end{aligned}$$

where the following notation in Eqs.(1) was used for conciseness,

$$\begin{aligned}
\boldsymbol{g}^T_{\breve{\boldsymbol{q}},n+1} &= \boldsymbol{g}^T_{\breve{\boldsymbol{q}}}(\breve{\boldsymbol{q}}_{n+1}) && (2)\\
\boldsymbol{f}^p &= \boldsymbol{f}(\boldsymbol{q}_{n+1}, \breve{\boldsymbol{v}}_{n+1}, t_{n+1}) - \boldsymbol{f}(\breve{\boldsymbol{q}}_{n+1}, \breve{\boldsymbol{v}}_{n+1}, t_{n+1}) - \boldsymbol{g}^{\overline{\mathcal{U}}\,T}_{\breve{\boldsymbol{q}},n+1}\,\breve{\boldsymbol{\lambda}}^{\overline{\mathcal{U}}}_{n+1} && (3)\\
\boldsymbol{f}^v &= \boldsymbol{f}(\boldsymbol{q}_{n+1}, \boldsymbol{v}_{n+1}, t_{n+1}) - \boldsymbol{f}(\breve{\boldsymbol{q}}_{n+1}, \breve{\boldsymbol{v}}_{n+1}, t_{n+1}) - \boldsymbol{g}^{\overline{\mathcal{U}}\,T}_{\breve{\boldsymbol{q}},n+1}\,\breve{\boldsymbol{\lambda}}^{\overline{\mathcal{U}}}_{n+1} && (4)
\end{aligned}$$

Equations (1)-a-b are the momentum balance and bilateral constraints (smooth contribution), meanwhile Eqs.(1)-c-d-e and Eqs.(1)-f-g-h give the position and velocity corrections of motion due to impacts: $\boldsymbol{U}_{n+1}$ and $\boldsymbol{W}_{n+1}$, respectively. Then, t is the time, h is the time step size, $\boldsymbol{M}$ is the mass matrix, $\boldsymbol{g}$ is the combined set of bilateral and unilateral constraints, $\boldsymbol{g}_{\boldsymbol{q}}(\breve{\boldsymbol{q}})$ is the gradient of $\boldsymbol{g}$ and $\mathring{\boldsymbol{g}}$ is the Newton's law which will be defined in Sec. 3. The variable $\breve{\boldsymbol{\lambda}}$ is a Lagrange multiplier vector associated to the bilateral restriction, and $\breve{\boldsymbol{q}}_{n+1}$, $\breve{\boldsymbol{v}}_{n+1}$ and $\dot{\breve{\boldsymbol{v}}}$ are the position, the velocity and the acceleration vectors of the system, respectively. These variables are the contributions of the smooth problem, i.e. they are solution of the problem without considering impacts. The position jumps contribution $\boldsymbol{U}_{n+1}$ due to impact is associated with the Lagrange multiplier $\boldsymbol{\nu}_{n+1}$ for the unilateral and bilateral constraints. The Lagrange multiplier $\boldsymbol{\Lambda}$ represents an impulsive force that can be interpreted as the integral of the reactions in the time interval $(t_n, t_{n+1}]$ and $\boldsymbol{W}_{n+1}$ is the velocity correction. Then, taking into account the splitting of motion into a smooth and a nonsmooth contributions, the physical displacement and velocity fields are computed by adding the correction vectors $\boldsymbol{U}_{n+1}$ and $\boldsymbol{W}_{n+1}$ to the smooth parts of motion as follows,

$$\boldsymbol{q}_{n+1} = \breve{\boldsymbol{q}}_{n+1} + \boldsymbol{U}_{n+1} \tag{5a}$$
$$\boldsymbol{v}_{n+1} = \breve{\boldsymbol{v}}_{n+1} + \boldsymbol{W}_{n+1} \tag{5b}$$

where $\boldsymbol{q}$ is the vector of nodal coordinates and $\boldsymbol{v}$ is the nodal velocity assumed to be of bounded variation. The penalty factors $p_s > 0$, $p_p > 0$, $p_v > 0$ of the smooth, position and velocity problems are used to improve the convergence rate, while the scaling factors $k_s > 0$, $k_p > 0$ and $k_v > 0$ contribute to an improvement of the condition number of the iteration matrix. They are chosen as $k_s = p_s = \bar{m}/h$, $k_p = p_p = \bar{m}$ and $k_v = p_v = \bar{m}$ giving a good scaling of equations where $\bar{m}$ is a characteristic mass of the problem. The integration algorithm is completed with the following difference equations of the generalized–α scheme

$$\breve{\boldsymbol{q}}_{n+1} = \boldsymbol{q}_n + h\boldsymbol{v}_n + h^2(0.5-\beta)\boldsymbol{a}_n + h^2\beta\boldsymbol{a}_{n+1} \tag{6a}$$
$$\breve{\boldsymbol{v}}_{n+1} = \boldsymbol{v}_n + h(1-\gamma)\boldsymbol{a}_n + h\gamma\boldsymbol{a}_{n+1} \tag{6b}$$
$$(1-\alpha_m)\boldsymbol{a}_{n+1} + \alpha_m\boldsymbol{a}_n = (1-\alpha_f)\dot{\breve{\boldsymbol{v}}}_{n+1} + \alpha_f\dot{\boldsymbol{v}}_n \tag{6c}$$

where $\boldsymbol{a}_{n+1}$ is a pseudo acceleration term. The numerical coefficients γ, β, α_m, and α_f are selected by imposing the spectral radius at infinity $\rho_\infty \in [0, 1)$,

$$\alpha_m = \frac{2\rho_\infty - 1}{\rho_\infty + 1}, \quad \alpha_f = \frac{\rho_\infty}{\rho_\infty + 1}, \quad \gamma = 0.5 + \alpha_f - \alpha_m, \quad \beta = 0.25(\gamma + 0.5)^2 \tag{7}$$

Then, $\mathcal{U}$ denotes the set of indices of the unilateral constraints, $\overline{\mathcal{U}}$ is its complementarity set, i.e., the set of bilateral constraints and $\mathcal{C} = \mathcal{U} \cup \overline{\mathcal{U}}$ is the full set of constraints. The set of active unilateral constraints $\mathcal{A} \equiv \mathcal{A}_{n+1}$ and bilateral constraints and $\mathcal{B} \equiv \mathcal{B}_{n+1}$, together with their complementary sets $\overline{\mathcal{A}}_{n+1} \equiv \overline{\mathcal{A}}_{n+1}$ and $\overline{\mathcal{B}}_{n+1} \equiv \overline{\mathcal{B}}_{n+1}$, are defined in the following form

$$\mathcal{A}_{n+1} = \overline{\mathcal{U}} \cup \left\{ j \in \mathcal{U} : k_p\boldsymbol{\nu}^j_{n+1} - p_p\boldsymbol{g}^j_{n+1} \geq 0 \right\} \tag{8a}$$
$$\overline{\mathcal{A}}_{n+1} = \mathcal{C} \setminus \mathcal{A}_{n+1} \tag{8b}$$
$$\mathcal{B}_{n+1} = \overline{\mathcal{U}} \cup \{ j \in \mathcal{A}_{n+1} : k_v\boldsymbol{\Lambda}^j_{n+1} - p_v\mathring{\boldsymbol{g}}^j_{n+1} \geq 0 \} \tag{8c}$$
$$\overline{\mathcal{B}}_{n+1} = \mathcal{C} \setminus \mathcal{B}_{n+1} \tag{8d}$$

Then, the residual vectors $\boldsymbol{r}^s$, $\boldsymbol{r}^p$,$\boldsymbol{r}^v$ of the smooth, position and velocity sub-problems are obtained from the imbalance of Eqs.(1)-ab, Eqs.(1)-cde, and Eqs.(1)-fgh, respectively. By defining the generalized unknown vectors

$$\Delta\boldsymbol{x}^s = \left\{ \begin{array}{c} \Delta\breve{\boldsymbol{v}}_{n+1} \\ \Delta\breve{\boldsymbol{\lambda}}^{\overline{\mathcal{U}}}_{n+1} \end{array} \right\}, \quad \Delta\boldsymbol{x}^p = \left\{ \begin{array}{c} \Delta\boldsymbol{U}_{n+1} \\ \Delta\boldsymbol{\nu}^{\mathcal{A}}_{n+1} \\ \Delta\boldsymbol{\nu}^{\overline{\mathcal{A}}}_{n+1} \end{array} \right\}, \text{ and } \quad \Delta\boldsymbol{x}^v = \left\{ \begin{array}{c} \Delta\boldsymbol{W}_{n+1} \\ \Delta\boldsymbol{\Lambda}^{\mathcal{B}}_{n+1} \\ \Delta\boldsymbol{\Lambda}^{\overline{\mathcal{B}}}_{n+1} \end{array} \right\}, \tag{9}$$

the iterative correction equations for each sub-problem are evaluated as follows

$$\boldsymbol{S}^i_t\,\Delta\boldsymbol{x}^i = -\boldsymbol{r}^i, \quad \text{for} \quad i = s, p, v \tag{10}$$

where the iteration matrices are:

$$\boldsymbol{S}_t^s = \begin{bmatrix} \boldsymbol{S}_t^{s^*} & -k_s \boldsymbol{g}_{\check{\boldsymbol{q}},n+1}^{\overline{\mathcal{U}},T} \\ -k_s \left(\boldsymbol{g}_{\check{\boldsymbol{q}},n+1}^{\overline{\mathcal{U}}} + \frac{h\beta}{\gamma} \boldsymbol{G}^s \right) & \boldsymbol{0} \end{bmatrix} \tag{11}$$

$$\boldsymbol{S}_t^p = \begin{bmatrix} \boldsymbol{S}_t^{p^*} & -k_p \boldsymbol{g}_{\boldsymbol{q},n+1}^{\mathcal{A},T} & \boldsymbol{0} \\ -k_p \boldsymbol{g}_{\boldsymbol{q},n+1}^{\mathcal{A}} & \boldsymbol{0} & \boldsymbol{0} \\ \boldsymbol{0} & \boldsymbol{0} & -\frac{k_p^2}{p_p} \boldsymbol{I}^{\overline{\mathcal{A}}} \end{bmatrix} \tag{12}$$

$$\boldsymbol{S}_t^v = \begin{bmatrix} \boldsymbol{S}_t^{v^*} & -k_v \boldsymbol{g}_{\boldsymbol{q},n+1}^{\mathcal{B},T} & \boldsymbol{0} \\ -k_v \boldsymbol{g}_{\boldsymbol{q},n+1}^{\mathcal{B}} & \boldsymbol{0} & \boldsymbol{0} \\ \boldsymbol{0} & \boldsymbol{0} & -\frac{k_v^2}{p_v} \boldsymbol{I}^{\overline{\mathcal{B}}} \end{bmatrix} \tag{13}$$

where $\boldsymbol{I}^{\overline{\mathcal{A}}}$. In practice, the Newton scheme is complemented with a line-search strategy to improve the robustness of the resulting algorithm. The complete description of the integrator is not given here for conciseness, more details can be found in [20] with the full expressions of the tangent matrices. The pseudocode is given in the Appendix A. An extension of this algorithm for handling frictionless multiple impact collisions can be found in [19].

3 Frictional Contact Formulation

The kinematics of two contacting bodies with friction effects is described in terms of the gap distance between the potential contact surfaces. It is usually split into a normal and a tangential component: $g_N \in \mathbb{R}$ and $\boldsymbol{g}_T = [g_{T1}\ g_{T2}]^T \in \mathbb{R}^2$, referred to a material orthonormal frame at the contact point, respectively. The same procedure is performed with the contact force $\boldsymbol{\nu}$, which is decomposed into a normal component $\nu_N \in \mathbb{R}$ and a tangential component $\boldsymbol{\nu}_T = [\nu_{T1}\ \nu_{T2}] \in \mathbb{R}^2$. This splitting allows to define the restrictions of gap, contact, stick or slip of the frictional contact problem at position level as follows:

$$\begin{array}{ccc} g_N \geq 0 & \nu_N \geq 0, & g_N \nu_N = 0; \\ \|\boldsymbol{g}_T\| \geq 0, & \|\boldsymbol{\nu}_T\| \leq \mu \nu_N, & \|\boldsymbol{g}_T\| \left(\|\boldsymbol{\nu}_T\| - \mu \nu_N \right) = 0 \end{array} \tag{14}$$

where μ is the friction coefficient, and where the associative slip rule $\|\boldsymbol{\nu}_T\|\ \boldsymbol{g}_T = -\|\boldsymbol{g}_T\|\ \boldsymbol{\nu}_T$ also holds. The first set of inequality equations of Eq.(14) represents the normal contact conditions telling if the bodies are in *gap* or in *contact* status. The second set corresponds to the Coulomb's friction law which states whether the bodies are in *stick* or in *slip* status.

The set of inequality constraints in Eq.(14) can be enforced using an augmented Lagrangian formulation as proposed Alart and Curnier[4]. The adopted augmented Lagrangian function for the frictional contact problem at position level, in terms of the nodal coordinates vector $\boldsymbol{q}$ and contact forces $\boldsymbol{\nu}$, is given by

$$\mathcal{L}^p(\boldsymbol{q}, \boldsymbol{\nu}) = -k_p g_N \nu_N + \frac{p_p}{2} g_N^2 - \frac{\mathrm{dist}^2}{2p_p} \left[\xi_N, \mathbb{R}^+ \right] - k_p \boldsymbol{g}_T \cdot \boldsymbol{\nu}_T + \frac{p_p}{2} \|\boldsymbol{g}_T\|^2 - \frac{\mathrm{dist}^2 \left[\boldsymbol{\xi}_T, C_{\xi_N} \right]}{2p_p} \tag{15}$$

where $\xi_N = k_p \nu_N - p_p g_N$ and $\boldsymbol{\xi}_T = k_p \boldsymbol{\nu}_T - p_p \boldsymbol{g}_T$ are the augmented multipliers for the normal and the tangential direction at position level, respectively; p_p is a positive penalty parameter and k_p is a scaling factor for the Lagrange multipliers ν_N and $\boldsymbol{\nu}_T$. Function $\mathrm{dist}(\boldsymbol{z}, C)$ is the distance between a point $\boldsymbol{z} \in \mathbb{R}^n$ and the convex set C, while the cone C_{ξ_N} is the convex set defined by the extension of the friction cone $C(k_p \nu_N + p_p g_N) \equiv C(\xi_N)$ to the half-line $\mathbb{R}^-(\xi_N)$, i.e. the set of negative values of the normal augmented multiplier $\xi_N = k_p \nu_N + p_p g_N$ (more details can be found in [43]). Note that $\boldsymbol{g}_T$ is the tangential component of the incremental relative displacement between points in contact during the considered time step.

We define the terms $\mathring{g}_N \in \mathbb{R}$ and $\mathring{\boldsymbol{g}}_T \in \mathbb{R}^2$ to express the Newton impact's law in the normal and tangential directions, as follows,

$$\mathring{g}_N = g_{N\boldsymbol{q},n+1}\boldsymbol{v}_{n+1} + e_N g_{N\boldsymbol{q},n}\boldsymbol{v}_n \qquad \mathring{\boldsymbol{g}}_T = \boldsymbol{g}_{T\boldsymbol{q},n+1}\boldsymbol{v}_{n+1} + e_T \boldsymbol{g}_{T\boldsymbol{q},n}\boldsymbol{v}_n \tag{16}$$

Here, $e_N \in [0,1]$ and $e_T \in (-1,1)$ are the coefficients of restitution in the normal and tangential directions, respectively, and $g_{N\boldsymbol{q}}$ and $\boldsymbol{g}_{T\boldsymbol{q}}$ are the gradients of the normal and incremental tangential displacements, respectively. Then, the frictional contact conditions at velocity level are written in analogous form as Eq.(14) yielding,

$$\begin{aligned} \mathring{g}_N &\geq 0, \qquad & \Lambda_N &\geq 0, \qquad & \mathring{g}_N \Lambda_N &= 0; \\ \|\mathring{\boldsymbol{g}}_T\| &\geq 0, \qquad & \|\boldsymbol{\Lambda}_T\| &\leq \mu \Lambda_N, \qquad & \|\mathring{\boldsymbol{g}}_T\| \left(\|\boldsymbol{\Lambda}_T\| - \mu \Lambda_N\right) &= 0 \end{aligned} \tag{17}$$

where the associative rule $\|\boldsymbol{\Lambda}_T\| \; \mathring{\boldsymbol{g}}_T = -\|\mathring{\boldsymbol{g}}_T\| \; \boldsymbol{\Lambda}_T$ holds, and where $\Lambda_N \in \mathbb{R}$ and $\boldsymbol{\Lambda}_T = [\Lambda_1 \; \Lambda_2]^T \in \mathbb{R}^2$ are the normal and the tangential impulses in the normal and tangential directions, respectively, with respect to an orthonormal material frame located at the contact point. Then, similarly to Eq.(15), the augmented Lagrangian for the frictional contact problem at velocity level is given by

$$\mathcal{L}^v(\boldsymbol{v}, \boldsymbol{\Lambda}) = -k_v \mathring{g}_N \Lambda_N + \frac{p_v}{2}\mathring{g}_N^2 - \frac{\mathrm{dist}^2\left[\sigma_N, \mathbb{R}^+\right]}{2p_v} - k_v \mathring{\boldsymbol{g}}_T \cdot \boldsymbol{\Lambda}_T + \frac{p_v}{2}\|\mathring{\boldsymbol{g}}_T\|^2 - \frac{\mathrm{dist}^2\left[\boldsymbol{\sigma}_T, C_{\sigma_N}\right]}{2p_v} \tag{18}$$

where $\sigma_N = k_v \Lambda_N - p_v \mathring{g}_N$ and $\boldsymbol{\sigma}_T = k_v \boldsymbol{\Lambda}_T - p_v \mathring{\boldsymbol{g}}_T$ are the augmented multipliers at velocity level in the normal and tangential directions, respectively and C_{σ_N} is a section of radius $\mu\sigma_N$ of the augmented Coulomb friction cone expressed in terms of velocity variables. Then, p_v is a positive penalty parameter and k_v is the scaling factor for the Lagrange multipliers Λ_N and $\boldsymbol{\Lambda}_T$.

The virtual variations of the augmented Lagrangians (15,18) give the internal forces vectors, and their linearisation yields the corresponding Hessian matrices. They are calculated in the next subsection.

3.1 Internal Forces Vectors and Hessian Matrices

The contact elements contribute only via unilateral constraints to the position and velocity correction equations, or in other words, they do not contribute to the smooth motion subproblem. In what follows, the indices n or $n+1$ will be omitted from the equations to simplify the notation. The generalized internal force vector at position level is obtained by taking variations in the augmented Lagrangian $\mathcal{L}^p$ of Eq.(15) giving

$$\delta\mathcal{L}^p(\boldsymbol{q}, \boldsymbol{\nu}) = -k_p \delta\nu_N g_N - \xi_N \delta g_N - \frac{1}{p_p}\,\delta\Big(\frac{1}{2}\mathrm{dist}^2(\xi_N, \mathbb{R}^+)\Big) - k_p \delta\boldsymbol{\nu}_T \cdot \boldsymbol{g}_T - \boldsymbol{\xi}_T \cdot \delta\boldsymbol{g}_T - \frac{1}{p_p}\,\delta\Big(\frac{1}{2}\mathrm{dist}^2(\boldsymbol{\xi}_T, C_{\xi_N})\Big) \tag{19}$$

Details about the variations of the terms in Eq. (19) can be found in Sánchez *et al* [60]. Then, by defining the generalized coordinates vector $\boldsymbol{\Phi} = [\boldsymbol{q}^T \; \nu_N \; \boldsymbol{\nu}_T^T]^T$, the variation of the augmented Lagrangian is written as follows

$$\delta\mathcal{L}^p(\boldsymbol{\Phi}) = \delta\boldsymbol{\Phi}^T \boldsymbol{F}^p(\boldsymbol{\Phi}) \tag{20}$$

where the internal force vector at position level for the different contact status is given by

$$\boldsymbol{F}^p(\boldsymbol{\Phi}) = \begin{cases} \begin{Bmatrix} \mathbf{0} \\ -\frac{k_p^2}{p_p}\nu_N \\ -\frac{k_p^2}{p_p}\boldsymbol{\nu}_T \end{Bmatrix} & \xi_N < 0 \quad \text{Gap} \\ \begin{Bmatrix} -g_{N\boldsymbol{q}}^T\xi_N - \mu\xi_N\boldsymbol{g}_{T\boldsymbol{q}}^T\boldsymbol{\tau}_p \\ -k_p g_N \\ \frac{k_p}{p_p}(-k_p\boldsymbol{\nu}_T + \mu\xi_N\boldsymbol{\tau}_p) \end{Bmatrix} & \|\boldsymbol{\xi}_T\| \geq \mu\xi_N \quad \text{Slip} \\ \begin{Bmatrix} -g_{N\boldsymbol{q}}^T\xi_N - \boldsymbol{g}_{T\boldsymbol{q}}^T\boldsymbol{\xi}_T \\ -k_p g_N \\ -k_p\boldsymbol{g}_T \end{Bmatrix} & \|\boldsymbol{\xi}_T\| < \mu\xi_N \quad \text{Stick} \end{cases} \tag{21}$$

where $\boldsymbol{\tau}_p = \boldsymbol{\xi}_T/\|\boldsymbol{\xi}_T\|$ is a unit vector that defines the tangential direction of the contact force. The linearization of the internal force vectors at position level yields the contact Hessian matrix for the different contact conditions (see details in [60]).

By following a similar reasoning as in the position level subproblem, the variation of the augmented Lagrangian at velocity level is calculated from Eq.(18) giving

$$\delta\mathcal{L}^v\boldsymbol{\Phi}) = \delta\boldsymbol{\Phi}^T\boldsymbol{F}^v(\boldsymbol{\Phi}) \tag{22}$$

Then, from Eq.(22), the internal force vectors at velocity level for the contact status are given by

$$\boldsymbol{F}^v(\boldsymbol{\Phi}) = \begin{cases} \begin{Bmatrix} \boldsymbol{0} \\ -\frac{k_v^2}{p_v}\Lambda_N \\ -\frac{k_v^2}{p_v}\boldsymbol{\Lambda}_T \end{Bmatrix} & \sigma_N < 0 \quad \text{Gap} \\ \begin{Bmatrix} -g_{N\boldsymbol{q}}^T\sigma_N - \mu\sigma_N\boldsymbol{g}_{T\boldsymbol{q}}^T\boldsymbol{\tau}_v \\ -k_v \mathring{g}_N \\ \frac{k_v}{p_v}(-k_v\boldsymbol{\Lambda}_T + \mu\sigma_N\boldsymbol{\tau}_v) \end{Bmatrix} & \|\boldsymbol{\sigma}_T\| \geq \mu\sigma_N \quad \text{Slip} \\ \begin{Bmatrix} -g_{N\boldsymbol{q}}^T\sigma_N - \boldsymbol{g}_{T\boldsymbol{q}}^T\boldsymbol{\sigma}_T \\ -k_v \mathring{g}_N \\ -k_v\mathring{\boldsymbol{g}}_T \end{Bmatrix} & \|\boldsymbol{\sigma}_T\| < \mu\sigma_N \quad \text{Stick} \end{cases} \tag{23}$$

where $\boldsymbol{\tau}_v = \boldsymbol{\sigma}_T/\|\boldsymbol{\sigma}_T\|$ is a unit vector that defines the tangential direction of the contact force at velocity level. The Hessian matrices are obtained by a linearization of the internal contact force vectors at velocity level (see [60]).

The internal force vectors and Hessian matrices have been developed in a completely general form, without particularizing to any contact model. They depend on the definition of the gap distance vector and the gradient matrices in the normal and tangential directions.

3.2 Multiple Impacts Collisions

In the case of collisions with multiple frictional impacts, a similar procedure is applied which iterates over a sequence of impact problems on a vanishing time interval until no further impact is detected. This formulation, which exploits a modified activation criterion at velocity level, is based on the recent work presented by Cosimo *et al.* [19].

The first iteration is equivalent to the procedure already described. Variables $\boldsymbol{V}^-$ and $\breve{\boldsymbol{V}}^-$ are introduced, which respectively represent the updated expressions of the pre-impact velocities $\boldsymbol{v}_n$ and $\breve{\boldsymbol{v}}_{n+1}$ for the next iterations. The Newton impact law in the normal and tangential directions is defined in terms of $\boldsymbol{V}^-$ as

$$\mathring{g}^{*\,j}_{N,n+1} = g^j_{N\boldsymbol{q},n+1}\boldsymbol{v}_{n+1} + e^j_N g^j_{N\boldsymbol{q},n}\boldsymbol{V}^- \qquad \mathring{\boldsymbol{g}}^{*\,j}_{T,n+1} = \boldsymbol{g}^j_{T\boldsymbol{q},n+1}\boldsymbol{v}_{n+1} + e^j_T \boldsymbol{g}^j_{T\boldsymbol{q},n}\boldsymbol{V}^- \tag{24}$$

These computations are performed for every impact point $j \in \mathcal{C}$. Accordingly, the modified augmented multiplier involved by the sub-problem at velocity level is denoted by $\boldsymbol{\sigma}^*_{n+1}$:

$$\boldsymbol{\sigma}^*_{n+1} = \left\{ \begin{array}{c} k_v \Lambda_{N,n+1} - p_v \mathring{g}^*_{N,n+1} \\ k_v \boldsymbol{\Lambda}_{T,n+1} - p_v \mathring{\boldsymbol{g}}^*_{T,n+1} \end{array} \right\} \tag{25}$$

The modified active set is denoted by $\mathcal{G}^*$ and it is defined as

$$\mathcal{G}^*_{n+1} \;=\; \overline{\mathcal{U}} \cup \{ j \in \mathcal{A}_{n+1} : g^j_{\boldsymbol{q},n+1}\breve{\boldsymbol{V}}^- < \mathrm{tol}_{\boldsymbol{v}} \;\text{ and }\; \sigma^{*\,j}_{N,n+1} \geq 0 \} \tag{26}$$

where σ^*_N is the first row of vector in Eq.(25) which corresponds to the normal component of $\boldsymbol{\sigma}^*$. The condition $g^j_{\boldsymbol{q},n+1}\breve{\boldsymbol{V}}^- < \mathrm{tol}_{\boldsymbol{v}}$ asks for the admissibility of the pre-impact velocity. The other condition states that the augmented multiplier corresponding to the impact impulsion must be positive. Once an impact from the sequence is solved, the pre-impact velocities $\boldsymbol{V}^-$ and $\breve{\boldsymbol{V}}^-$ are updated taking into account the contribution of the just computed velocity jump $\boldsymbol{W}_{n+1}$,

$$\boldsymbol{V}^- \;=\; \boldsymbol{v}_n + \boldsymbol{W}_{n+1} \tag{27a}$$

$$\breve{\boldsymbol{V}}^- \;=\; \tilde{\boldsymbol{v}}_{n+1} + \boldsymbol{W}_{n+1} = \boldsymbol{v}_{n+1} \tag{27b}$$

This process continues until no more impacts take place in the sequence, which is equivalent to an empty active set $\mathcal{G}^*_{n+1}$. The velocity jump $\boldsymbol{W}_{n+1}$ should be here interpreted as the *total* jump which results from the accumulation of previously resolved impact problems from the generated sequence of impacts. Therefore, the resulting impulses are accumulated and taken into consideration in each impact problem of the sequence:

$$\boldsymbol{P}_N = \sum_j^{i-1} g^{\mathcal{G}^*_j,T}_{N\boldsymbol{q}} \Lambda^{\mathcal{G}^*_j}_N \qquad \boldsymbol{P}_T = \sum_j^{i-1} \boldsymbol{g}^{\mathcal{G}^*_j,T}_{T\boldsymbol{q}} \boldsymbol{\Lambda}^{\mathcal{G}^*_j}_T \tag{28}$$

where the index i is used to denote the impact problem from the sequence of impacts currently being solved.

Finally, the internal force vector for the velocity level sub-problem in the case of multiple frictional impacts is written as

$$\boldsymbol{F}^{v*,\mathcal{G}^*}(\boldsymbol{\Phi}) = \left\{ \begin{array}{ll} \left\{ \begin{array}{c} \boldsymbol{0} \\ -\frac{k_v^2}{p_v}\Lambda^{\mathcal{G}^*}_N \\ -\frac{k_v^2}{p_v}\boldsymbol{\Lambda}^{\mathcal{G}^*}_T \end{array} \right\} & \sigma^*_N < 0 \quad \text{Gap} \\ \left\{ \begin{array}{c} -g^{\mathcal{G}^*,T}_{N\boldsymbol{q}}\sigma^{*\mathcal{G}^*}_N - \mu\sigma^{*\mathcal{G}^*}_N \boldsymbol{g}^{\mathcal{G}^*,T}_{T\boldsymbol{q}}\boldsymbol{\tau}_v - \boldsymbol{P}_N - \boldsymbol{P}_T \\ -k_v \mathring{g}^{\mathcal{G}^*}_N \\ \frac{k_v}{p_v}(-k_v\boldsymbol{\Lambda}^{\mathcal{G}^*}_T + \mu\sigma^{\mathcal{G}^*}_N\boldsymbol{\tau}_v) \end{array} \right\} & \|\boldsymbol{\sigma}^*_T\| \geq \mu\sigma^*_N \quad \text{Slip} \\ \left\{ \begin{array}{c} -g^{\mathcal{G}^*,T}_{N\boldsymbol{q}}\sigma^{\mathcal{G}^*}_N - \boldsymbol{g}^{\mathcal{G}^*,T}_{T\boldsymbol{q}}\boldsymbol{\sigma}^{\mathcal{G}^*}_T - \boldsymbol{P}_N - \boldsymbol{P}_T \\ -k_v \mathring{g}^{\mathcal{G}^*}_N \\ -k_v \mathring{\boldsymbol{g}}^{\mathcal{G}^*}_T \end{array} \right\} & \|\boldsymbol{\sigma}^*_T\| < \mu\sigma^*_N \quad \text{Stick} \end{array} \right. \tag{29}$$

4 Sphere-Sphere Contact Model

The strategy that we adopted to develop a contact model for a rigid sphere in contact with another sphere, see Fig.1, follows the methodology given in [34]. The element takes into account sliding friction in the framework of nonsmooth contact dynamics with finite displacements and large rotations. The spheres are able to come in contact, rotate or slide one over the other. The motion is referred to an inertial frame (Fig. 1). The centres of spheres A and B, with

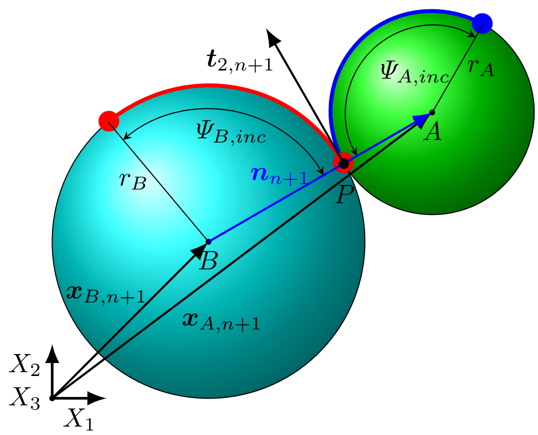

Figure 1: Configuration of the three-dimensional sphere-sphere contact model.

radius r_A, r_B, are given by position vectors $\boldsymbol{x}_A$ and $\boldsymbol{x}_B$, respectively. The description of motion of the spheres is completed by giving the rotation operators $\boldsymbol{R}_A, \boldsymbol{R}_B$ at each node, with the incremental rotation vector $\boldsymbol{\Psi}_{A,\text{incr}} \in \boldsymbol{R}^3$ from time t_n to time t_{n+1} given by

$$\exp(\tilde{\boldsymbol{\Psi}}_{A,\text{incr}}) = \boldsymbol{R}^T_{A,n}\boldsymbol{R}_{A,\text{n+1}} \tag{30}$$

where the exponential map $\exp(\tilde{\boldsymbol{\Psi}})$ is used. Here, $\boldsymbol{\Psi}_{A,\text{incr}} = \text{vect}(\tilde{\boldsymbol{\Psi}}_{A,\text{incr}})$ is the so-called Cartesian rotation vector which has the direction of the rotation axis and length equal to the amplitude of the incremental rotation [34]. Analogous equations can be derived for sphere B. The operator $\widetilde{\boldsymbol{a}} : \mathbb{R}^3 \to \mathbb{R}^3 \otimes \mathbb{R}^3$ gives a 3×3 skew-symmetric matrix such that $\boldsymbol{a}\times\boldsymbol{b} = \widetilde{\boldsymbol{a}}\boldsymbol{b}\ \forall\ \boldsymbol{a}, \boldsymbol{b} \in \mathbb{R}^3$.

The direction of contact between spheres is given by the unit vector $\boldsymbol{n}$, which is defined as

$$\boldsymbol{n} = \frac{\boldsymbol{x}_A - \boldsymbol{x}_B}{\parallel \boldsymbol{x}_A - \boldsymbol{x}_B \parallel} \tag{31}$$

In order to obtain the gap function of this element we define a material frame at the contact point P, using the normal vector $\boldsymbol{n}$ and the tangential vectors $\boldsymbol{t}_1$ and $\boldsymbol{t}_2$ which are defined as follows

$$\boldsymbol{t}_1 = \frac{\boldsymbol{e}\times\boldsymbol{n}}{\|\boldsymbol{e}\times\boldsymbol{n}\|} \qquad \boldsymbol{t}_2 = \boldsymbol{n}\times\boldsymbol{t}_1 \tag{32}$$

Here, $\boldsymbol{e}$ is an arbitrary vector not collinear with $\boldsymbol{n}$. The normal gap between the spheres is simply computed as

$$g_N = \parallel \boldsymbol{x}_A - \boldsymbol{x}_B \parallel -(r_A + r_B) \tag{33}$$

The contact status is established when the distance $\parallel \boldsymbol{x}_A - \boldsymbol{x}_B \parallel$ is equal to the sum of radii of the spheres $r_A + r_B$; otherwise, the spheres are not in contact. The velocities of the spheres

A and B at the contact point P are $\dot{\boldsymbol{x}}_{PA}(t)$ and $\dot{\boldsymbol{x}}_{PB}(t)$, respectively. They are calculated as follows

$$\dot{\boldsymbol{x}}_{PA}(t) = \dot{\boldsymbol{x}}_A(t) + \boldsymbol{n}(t) \times \boldsymbol{\omega}_A(t)\, r_A \qquad \dot{\boldsymbol{x}}_{PB}(t) = \dot{\boldsymbol{x}}_B(t) - \boldsymbol{n}(t) \times \boldsymbol{\omega}_B(t)\, r_B \tag{34}$$

We define the incremental tangential slip distance $\boldsymbol{g}_{T,n+1}$ between the spheres A and B, from time t_n to time t_{n+1}, as the integral of the relative velocity at the contact point: $\dot{\boldsymbol{x}}_{PA}(t)-\dot{\boldsymbol{x}}_{PB}(t)$ in the tangential directions $\boldsymbol{t}_1(t)$ and $\boldsymbol{t}_2(t)$:

$$\begin{aligned}\boldsymbol{g}_{T,n+1} = \begin{Bmatrix} g_{T1,n+1} \\ g_{T2,n+1} \end{Bmatrix} &= \int_{t_n}^{t_{n+1}} \begin{bmatrix} \boldsymbol{t}_1(t)^T \\ \boldsymbol{t}_2(t)^T \end{bmatrix} (\dot{\boldsymbol{x}}_{PA}(t) - \dot{\boldsymbol{x}}_{PB}(t))\ dt = \\ &= \int_{t_n}^{t_{n+1}} \begin{bmatrix} \boldsymbol{t}_1(t)^T \\ \boldsymbol{t}_2(t)^T \end{bmatrix} (\dot{\boldsymbol{x}}_A(t) - \dot{\boldsymbol{x}}_B(t) + \boldsymbol{n}(t) \times (\boldsymbol{\omega}_A(t) r_A + \boldsymbol{\omega}_B(t) r_B))\ dt\end{aligned} \tag{35}$$

After integration of Eq.(35), the following expression is obtained

$$\begin{Bmatrix} g_{T1,n+1} \\ g_{T2,n+1} \end{Bmatrix} = \begin{Bmatrix} \boldsymbol{t}_{1,n} \cdot [(\boldsymbol{x}_{A,n+1} - \boldsymbol{x}_{A,n}) - (\boldsymbol{x}_{B,n+1} - \boldsymbol{x}_{B,n}) + \boldsymbol{n}_n \times (\boldsymbol{\Psi}_{A,\mathrm{incr}} r_A + \boldsymbol{\Psi}_{B,\mathrm{incr}} r_B)] \\ \boldsymbol{t}_{2,n} \cdot [(\boldsymbol{x}_{A,n+1} - \boldsymbol{x}_{A,n}) - (\boldsymbol{x}_{B,n+1} - \boldsymbol{x}_{B,n}) + \boldsymbol{n}_n \times (\boldsymbol{\Psi}_{A,\mathrm{incr}} r_A + \boldsymbol{\Psi}_{B,\mathrm{incr}} r_B)] \end{Bmatrix} \tag{36}$$

where $\boldsymbol{t}_{\alpha,n} \cdot [(\boldsymbol{x}_{A,n+1} - \boldsymbol{x}_{A,n}) - (\boldsymbol{x}_{B,n+1} - \boldsymbol{x}_{B,n})]$ is the tangential relative displacements produced by the displacement of the spheres in space. Meanwhile, $\boldsymbol{t}_{\alpha,n} \cdot [\boldsymbol{n}_n \times (\boldsymbol{\Psi}_{A,\mathrm{incr}} r_A + \boldsymbol{\Psi}_{B,\mathrm{incr}} r_B)]$ with $\alpha = 1, 2$ can be interpreted as the tangential relative displacements produced by the rotation of the spheres. Note that in Eq.(36) the normal and tangential vectors are evaluated at the previous time step in order to facilitate the convergence and the internal force vectors and tangential matrices derivations. Refined formula may be considered, e.g., by using SE(3) integration [8]. Nevertheless, convergence of the nonlinear problem may then become more difficult. We remark that the simplification of evaluating the normal and the tangential vectors at previous time step does not affect the accuracy of the numerical solutions as we will demonstrate in the examples. In the Appendix B, a numerical experiment is presented in order to know the range of validity of Eq.(36). Finally, the generalized gap vector is defined as

$$\boldsymbol{g}_{n+1} = \begin{bmatrix} g_{N,n+1} \\ \boldsymbol{g}_{T,n+1} \end{bmatrix} = \begin{bmatrix} \|\boldsymbol{x}_{A,n+1} - \boldsymbol{x}_{B,n+1}\| - (r_A + r_B) \\ \boldsymbol{t}_{1,n} \cdot [(\boldsymbol{x}_{A,n+1} - \boldsymbol{x}_{B,n+1}) - (\boldsymbol{x}_{A,n} - \boldsymbol{x}_{B,n})] - \boldsymbol{t}_{2,n} \cdot (\boldsymbol{\Psi}_{A,\mathrm{incr}} r_A + \boldsymbol{\Psi}_{B,\mathrm{incr}} r_B) \\ \boldsymbol{t}_{2,n} \cdot [(\boldsymbol{x}_{A,n+1} - \boldsymbol{x}_{B,n+1}) - (\boldsymbol{x}_{A,n} - \boldsymbol{x}_{B,n})] + \boldsymbol{t}_{1,n} \cdot (\boldsymbol{\Psi}_{A,\mathrm{incr}} r_A + \boldsymbol{\Psi}_{B,\mathrm{incr}} r_B) \end{bmatrix} \tag{37}$$

where the circular-shift properties and the anti-commutativity of the cross-product for the scalar triple product were used to simplify the expressions.

The variation of the normal gap is given by

$$\delta g_N = g_{N\boldsymbol{q},n+1} \delta \boldsymbol{q} \tag{38}$$

where $\delta \boldsymbol{q}$ is the variation of the generalized coordinates vector $\delta \boldsymbol{q} = [\delta \boldsymbol{x}_A^T\ \delta \boldsymbol{x}_B^T\ \delta \boldsymbol{\Theta}_A^T\ \delta \boldsymbol{\Theta}_B^T]^T$; here, $\delta \boldsymbol{x}_A$ and $\delta \boldsymbol{x}_B$ are the variations of the position vectors whilst $\delta \boldsymbol{\Theta}_A$ and $\delta \boldsymbol{\Theta}_B$ are the incremental material rotations at nodes A and B, respectively. The normal gap gradients matrix of the element is

$$g_{N\boldsymbol{q},n+1} = \begin{bmatrix} \boldsymbol{n}_{n+1}^T & -\boldsymbol{n}_{n+1}^T & \boldsymbol{0}^T & \boldsymbol{0}^T \end{bmatrix} \tag{39}$$

By taking virtual variations of the incremental tangential displacements $\boldsymbol{g}_{T,n+1}$, Eq.(36), we get

$$\delta \boldsymbol{g}_T = \boldsymbol{g}_{T\boldsymbol{q},n} \delta \boldsymbol{q} \tag{40}$$

where $\boldsymbol{g}_{T\boldsymbol{q},n}$ is the gradients matrix for the tangential displacements, which is computed as follows

$$\boldsymbol{g}_{T\boldsymbol{q},n} = \begin{bmatrix} \boldsymbol{t}_{1,n}^T & -\boldsymbol{t}_{1,n}^T & -r_A\boldsymbol{t}_{2,n}^T & -r_B\boldsymbol{t}_{2,n}^T \\ \boldsymbol{t}_{2,n}^T & -\boldsymbol{t}_{2,n}^T & r_A\boldsymbol{t}_{1,n}^T & r_B\boldsymbol{t}_{1,n}^T \end{bmatrix} \tag{41}$$

At this point, all the expressions necessary to evaluate the internal force vectors at position level for this element have been computed, see Eq.(21).

In order to obtain the Hessian matrix at position level, the calculation of $\Delta g_{N\boldsymbol{q},n+1}^T$ is required. It yields the final expression,

$$g_{N\boldsymbol{q},n+1}^T = \begin{bmatrix} \frac{\boldsymbol{I}-\boldsymbol{n}_{n+1}\otimes\boldsymbol{n}_{n+1}}{\|\boldsymbol{x}_{A,n+1}-\boldsymbol{x}_{B,n+1}\|} & -\frac{\boldsymbol{I}-\boldsymbol{n}_{n+1}\otimes\boldsymbol{n}_{n+1}}{\|\boldsymbol{x}_{A,n+1}-\boldsymbol{x}_{B,n+1}\|} & \boldsymbol{0} & \boldsymbol{0} \\ -\frac{\boldsymbol{I}-\boldsymbol{n}_{n+1}\otimes\boldsymbol{n}_{n+1}}{\|\boldsymbol{x}_{A,n+1}-\boldsymbol{x}_{B,n+1}\|} & \frac{\boldsymbol{I}-\boldsymbol{n}_{n+1}\otimes\boldsymbol{n}_{n+1}}{\|\boldsymbol{x}_{A,n+1}-\boldsymbol{x}_{B,n+1}\|} & \boldsymbol{0} & \boldsymbol{0} \end{bmatrix} \tag{42}$$

where the arrangement of this matrix is according to $\Delta\boldsymbol{q} = [\Delta\boldsymbol{x}_A^T\ \Delta\boldsymbol{x}_B^T\ \Delta\boldsymbol{\Theta}_A^T\ \Delta\boldsymbol{\Theta}_B^T]^T$. Furthermore, the linearization $\Delta\boldsymbol{g}_{T\boldsymbol{q}}^T = \boldsymbol{0}$ since this matrix is evaluated at the previous time step. The other terms needed for the calculation of the Hessian matrix at position level were presented before.

The internal force vectors at velocity level are computed following the same procedure. The expression of the Newton's impact law, which appears in the vectors in Eq.(22), takes the following form,

$$\begin{bmatrix} \mathring{g}_{N_{n+1}} \\ \mathring{g}_{T1_{n+1}} \\ \mathring{g}_{T2_{n+1}} \end{bmatrix} = \begin{bmatrix} \boldsymbol{n}_{n+1}\cdot(\boldsymbol{v}_{A,n+1}-\boldsymbol{v}_{B,n+1}) + e_N\boldsymbol{n}_n\cdot(\boldsymbol{v}_{A,n}-\boldsymbol{v}_{B,n}) \\ \boldsymbol{t}_{1,n}\cdot(\boldsymbol{v}_{A,n+1}-\boldsymbol{v}_{B,n+1}) - \boldsymbol{t}_{2,n}\cdot(\boldsymbol{\omega}_{A,n+1}r_A+\boldsymbol{\omega}_{B,n+1}r_B) + \\ \quad + e_T\left[\boldsymbol{t}_{1,n}\cdot(\boldsymbol{v}_{A,n}-\boldsymbol{v}_{B,n}) - \boldsymbol{t}_{2,n}\cdot(\boldsymbol{\omega}_{A,n}r_A+\boldsymbol{\omega}_{B,n}r_B)\right] \\ \boldsymbol{t}_{2,n}\cdot(\boldsymbol{v}_{A,n+1}-\boldsymbol{v}_{B,n+1}) + \boldsymbol{t}_{1,n}\cdot(\boldsymbol{\omega}_{A,n+1}r_A+\boldsymbol{\omega}_{B,n+1}r_B) + \\ \quad + e_T\left[\boldsymbol{t}_{2,n}\cdot(\boldsymbol{v}_{A,n}-\boldsymbol{v}_{B,n}) + \boldsymbol{t}_{1,n}\cdot(\boldsymbol{\omega}_{A,n}r_A+\boldsymbol{\omega}_{B,n}r_B)\right] \end{bmatrix} \tag{43}$$

At velocity level, the variable $\boldsymbol{q}$ coming from the solution of the position sub-problem is fixed, thus $\Delta g_{N\boldsymbol{q}} = \boldsymbol{0}$ and the complete gradient matrix is constant during the velocity iteration, see the step 3 of the algorithm presented in the Appendix A. Thus, the complete set of equations to compute the internal force vectors and the Hessian matrices at velocity level have been developed.

Finally, the Hessian matrices and the internal force vectors of the element both at position and velocity levels contribute to the global tangent matrices and to the generalized internal forces vectors by a standard assembly procedure.

5 Numerical Examples

The contact element developed in this work has been implemented in the finite element research code Oofelie [15]. Six numerical examples are presented to show the accuracy and robustness of the proposed methodology.

The convergence criterion used in the numerical examples is given by

$$\|\boldsymbol{r}^i\| < \text{tol}_r\Big(\sum_k \|\boldsymbol{r}_k^i\| + \text{tol}_f\Big) \qquad i = s, p, v \tag{44}$$

where tol_r is a given relative tolerance, $\boldsymbol{r}_k^i$ is the k-th term contributing to the residual $\boldsymbol{r}^i$ (i.e., the vectors of external forces, of internal forces, etc), tol_f is a reference value of tolerance, and $\|\cdot\|$ is the L^2 norm.

The error for the computation of convergence rates in the examples was evaluated as

$$\text{Error}(h) = \frac{\sum_{i=0}^{N} |f_i - f(t_i)|}{\sum_{i=0}^{N} |f(t_i)|} \tag{45}$$

where h is the time step, N is the number of steps, f_i is the numerical solution computed by our algorithm, $f(t_i)$ is the reference solution and $|\cdot|$ the L^1 norm. The reference solution is taken equal to the analytical solution when available; otherwise, the numerical solution corresponding to a very small time step is used as a reference.

5.1 Frictional Contact between Spheres

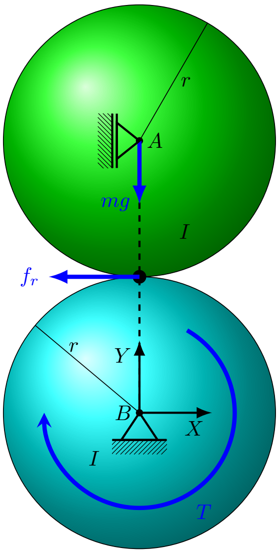

Figure 2: Validation example. Frictional spheres configuration.

This first simple example is used to validate the sphere-sphere contact element in a case of contact with friction. It consists of two touching spheres. The upper one A is free to rotate and to displace in the vertical direction, and is submitted to gravity $g = 9.8$ m/s^2, see Fig. 2. Sphere B is fixed at its centre and can rotate freely; rotation is imposed at sphere B with a time increasing torque law $T(t) = k\ t = 20\ t$ Nm. Both spheres remain in contact with a friction coefficient $\mu = 0.3$. The mass inertia moment of the spheres is $I = 0.4$ kg m^2, the mass is $m = 1$ kg and the radius is $r = 1$ m.

This problem has an analytical solution. For instance, the angular velocities and the angular displacements of the spheres are given as

$$\omega_A(t) = \begin{cases} \dfrac{kt^2}{4I} & \text{if } t \leq t_{lim} \\ \dfrac{kt_{lim}}{2I}\left(t - \dfrac{t_{lim}}{2}\right) & \text{if } t > t_{lim} \end{cases} \qquad \omega_B(t) = \begin{cases} -\dfrac{kt^2}{4I} & \text{if } t \leq t_{lim} \\ -\dfrac{k}{4I}\left(t_{lim}^2 + 2t(t - t_{lim})\right) & \text{if } t > t_{lim} \end{cases} \tag{46}$$

$$\theta_A(t) = \begin{cases} \dfrac{kt^3}{12I} & \text{if } t \leq t_{lim} \\ \dfrac{kt_{lim}t}{4I}(t - t_{lim}) + \dfrac{kt_{lim}^3}{12I} & \text{if } t > t_{lim} \end{cases} \qquad \theta_B(t) = \begin{cases} -\dfrac{kt^3}{12I} & \text{if } t \leq t_{lim} \\ -\dfrac{kt_{lim}t}{4I}(t - t_{lim}) + & \\ \frac{k}{6I}\left(\frac{kt_{lim}^3}{2} - t^3\right) & \text{if } t > t_{lim} \end{cases} \tag{47}$$

where $t_{lim} = 2mg\mu r/k$. The system is simulated for a total time 1 s with a constant time step 1×10^{-3} s. The tolerance for the nonlinear solver is fixed to 1×10^{-5} and the spectral ratio of the integrator is selected as $\rho_\infty = 0.8$. The numerical solution is given in Fig. 3. The contact force remains constant and is equal to the weight of sphere A, $f_c = mg = 9.8$ N, see Fig 3-a. The tangential force increases linearly reaching the maximum value of $f_T^{max} = \mu mg = 2.94$ N at time $t_{lim} = 0.294$ s; then, it remains constant when the spheres enter in slip state, see Fig. 3-a. The angular velocities of both spheres are equally accelerating and with opposite direction until time $t_{lim} = 0.294$ s while the contact status is stick. Then, velocity of the sphere B continues quadratically increasing in time because of the linearly increasing torque, while velocity of sphere A remains linearly increasing because of the slipping state which limits the transmitted torque to a constant value, see Fig. 3-b.

The maximum number of iterations per time-step in each sub-problem is 1, 3 and 3 with a mean number of 1, 2 and 2 iterations per time-step. Fig. 4 shows the computed convergence rate for the angular displacement and velocity of sphere A. The analytical solution was taken as reference, and a linear convergence rate is observed. No line search iterations were required to achieve convergence of the Newton scheme.

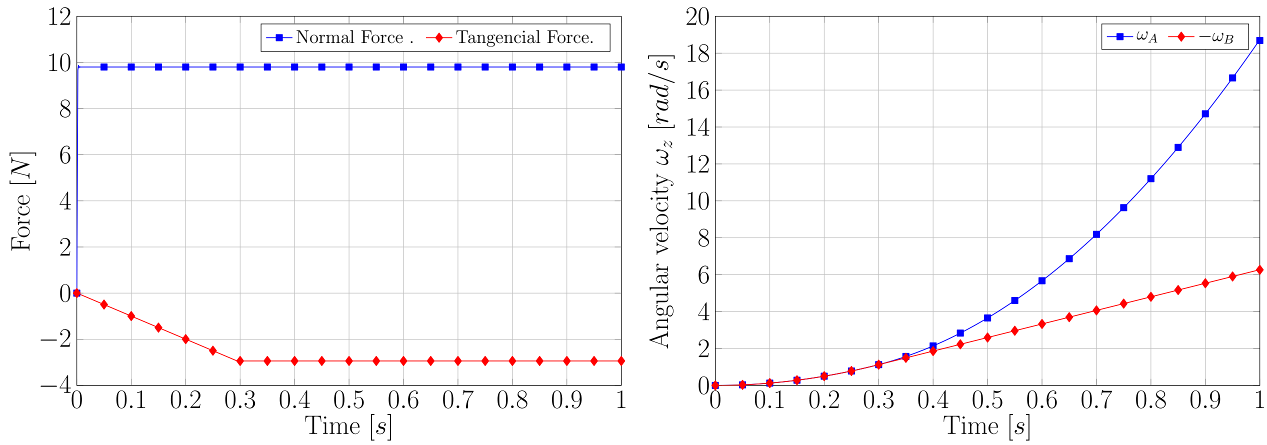

(a) Normal and tangential contact forces.

(b) Absolute value of angular velocities for spheres A and B.

Figure 3: Numerical solution for the frictional spheres example.

5.2 Single Collision Example

This case, which concerns the impact of two spheres, serves to validate the simulations of impact problems taking into account friction between the balls and the planar surface. The numerical solutions are compared against analytical solutions developed by Alciatore [7]. This example illustrates the 30° rule, which is well known in the billiard balls game. This rule states that if the cue ball in rolling motion impacts the target ball in rest at a point between 1/4-ball hit (49° cut) and 3/4-ball hit (14° cut), it will deflect by almost 30° from its original direction after hitting the target ball. When friction between balls is neglected and the coefficient of restitution is $e_N = 1$, the cue ball deflection angle θ_c as a function of the cut angle ϕ [7], is given by,

$$\theta_c = \tan^{-1}\left(\frac{\sin(\phi)\cos(\phi)}{\sin^2(\phi) + \frac{2}{5}}\right) \tag{48}$$

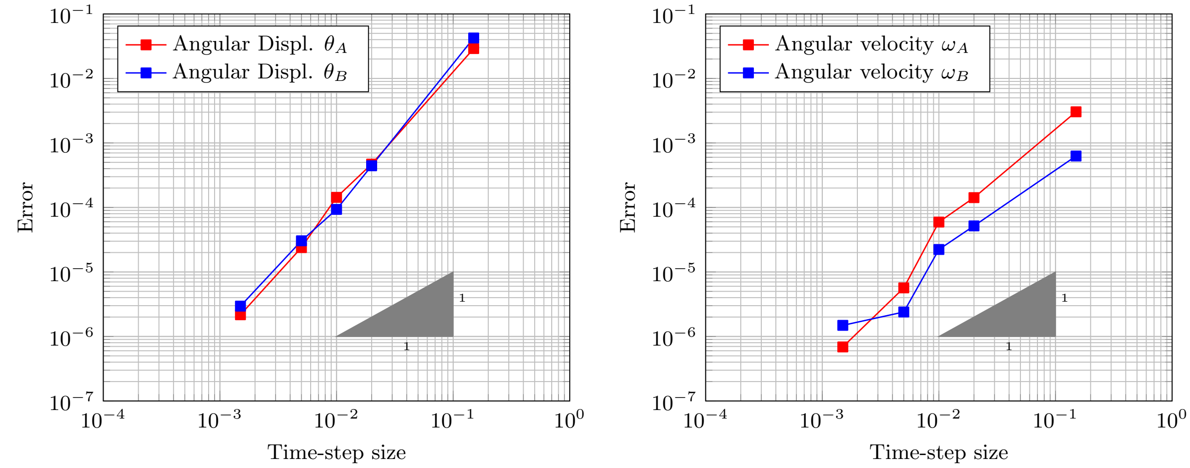

(a) Convergence rate for the Angular Displacement. (b) Convergence rate for the Angular Velocity.

Figure 4: Convergence rate for the frictional contact between spheres example.

where $\phi = \sin^{-1}(1-f)$ and f is the hit ball fraction factor $f \in [0, 1]$ between balls (see Figure 5-a). Comparisons of this analytical solution with experimental measurements can be found in [7, 62] and in many videos available in websites, showing good agreement. The geometrical and physical properties for the simulations, typical of the classical pool/billiard game, were selected from the book of Alciatore [7]. The radius of the balls are $r = 2.8575$ cm, the mass $m = 0.17$ kg and the coefficient of friction between the balls and the cloth is $\mu = 0.2$. The normal restitution coefficient value between the balls, and between the balls and the cloth, is $e_N = 1$. The tangential restitution coefficient is $e_T = 0$ for all contact points. The acceleration of gravity is $g = 9.8$ m/s^2.

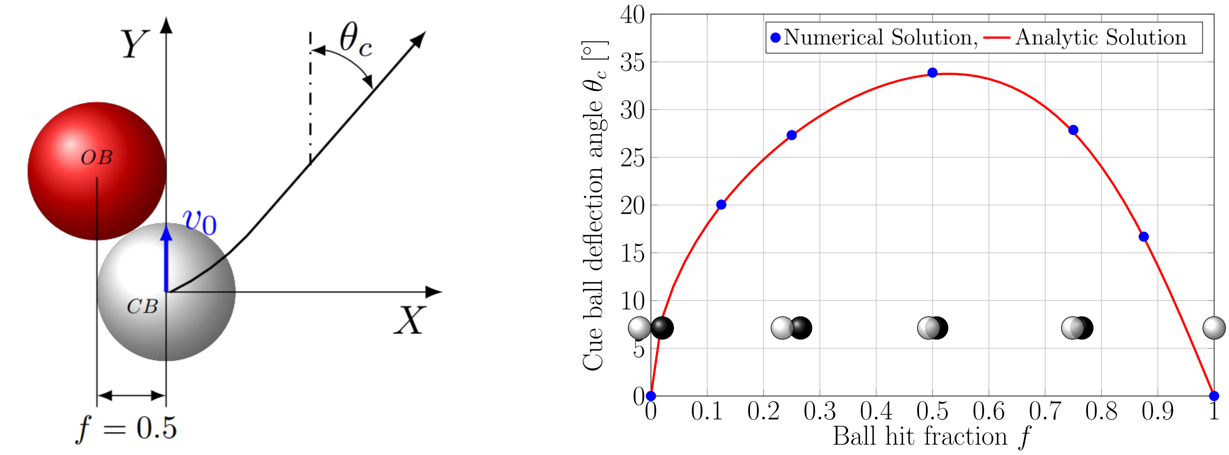

(a) The cue ball deflection angle θ_c. (b) The 30 °rule. Numerical and analytical solution comparison.

Figure 5: Impact between two spheres.

The cue ball impacts the target at a velocity $v^- = 1.8$ m/s in pure rolling motion. The numerical solution was computed with a time step $h = 1 \times 10^{-4}$ s and spectral radius $\rho_\infty = 0.8$. The value of tolerance for convergence was $\text{tol}_r = 1 \times 10^{-5}$. Computations for seven different hit ball fraction factors $f = [0, 0.125, 0.25, 0.5, 0.75, 0.875, 1]$ were performed. Figure 5-b shows the agreement between the analytical and the numerical solutions. The maximum number of iterations per time-step were 1, 4 and 5 with a mean number of 1 iteration per time-step for each sub-problem.

A second case more challenging than the previous one was considered, with friction between balls and restitution coefficient different from 1 [7]. The tangential component of the friction impulse was neglected, and the balls spinning velocity was imposed to be zero. With these assumptions, the trajectory of the cue ball immediately after impact can be described by the following set of equations,

$$\{x(t); y(t)\} = \begin{cases} \{x_c(t); y_c(t)\} & \text{if } t \leq t_{roll} \\ \{x_c(t_{roll}) + v_x(t_{roll})\,[t - t_{roll}]; y_c(t_{roll}) + v_y(t_{roll})\,[t - t_{roll}]\} & \text{if } t > t_{roll} \end{cases} \tag{49}$$

where t_{roll} is the time needed by the cue ball to stop sliding and enter into pure rolling motion after impact (see Appendix C, Eq. 65). The full set of equations necessary to calculate the evolution of the cue ball is given in Appendix C; the complete development can be found in [7].

Three cases with different values for the friction and restitution coefficients between balls, and hit fraction $f = 0.5$, were proposed to study the friction effects; they are: i) $\mu_{ball} = 0$, $e_N = 1$, ii) $\mu_{ball} = 0.06$, $e_N = 1$ and iii) $\mu_{ball} = 0$, $e_N = 0.94$. Figure 6-a displays the trajectory of the cue ball after impact calculated with Alciatore formulas and compared to the numerical solution of this work. From time 0 to t_{roll}, the cue ball describes a curved trajectory as a consequence of sliding with friction with the cloth; after that, when the ball is in a pure rolling motion, the trajectory is straight. Figure 6-a shows a good agreement between the analytical and numerical solutions.

Figure 6-b shows the analytical results compared with the numerical solutions computed when balls spinning is released, without being fixed to a zero value. We can observe that in this case we depart slightly from the trajectory calculated in [7]. The numerical solution was computed with a time step $h = 1 \times 10^{-4}$ s and spectral radius $\rho_\infty = 0.8$.

The displayed energy evolution is such that the system does not generate spurious energy throughout the simulation. Figure 7-a shows that, initially, the cue ball is in sliding movement with a reduction of kinetic energy. Subsequently, it enters in pure rolling motion conserving energy until collision with the object ball. At the moment of impact, the cue ball rebounds and separates from ground, as illustrated in Fig. 7-b, where an increase in potential energy is observed. Then, both balls change progressively from sliding to pure rolling motion reducing the total kinetic energy, as shown in Fig. 7-c. Finally, both balls move in pure rolling movement without losing energy.

The nonlinear problem at each time step was solved by Newton iterations, where the value of tolerance for convergence was $\text{tol}_r = 1 \times 10^{-5}$. The maximum number of iterations per time-step was 1, 4 and 5 for each subproblem, with a mean number of 1 iteration per time-step. Figure 8 illustrates the evolution of the logarithm of the residual norm, for the case $f = 0.5$, $e_N = 0.94$, $\mu_{ball} = 0.06$ without spin motion, at the step of impact for which the position and velocity iterations were activated. At impact instant, a quadratic convergence rate of the Newton iteration was obtained. In the first iteration of the Newton method, 3 iterations of line search at velocity level were required to convergence. In the remaining time steps, no line search iterations were required to achieve the convergence of the Newton scheme.

Finally, the convergence rate as a function of the time step, compared with the analytical solution, was calculated. The following set of parameters were used: $\mu_{ball} = 0.2$, $e_N = 0.94$, $\mu = 0.2$, $\omega_z = 0$ and $f = 0.5$. Figure 9 shows a linear convergence rate as expected.

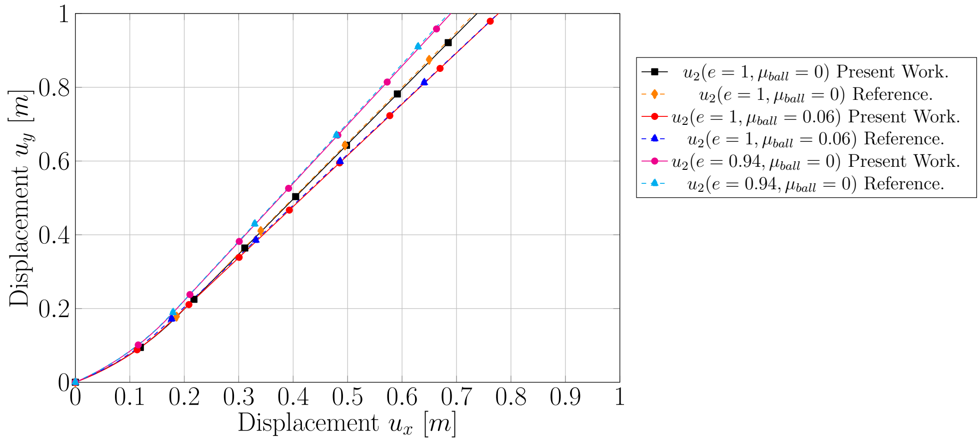

(a) Trajectory of the cue ball after impact with out considering spin motion.

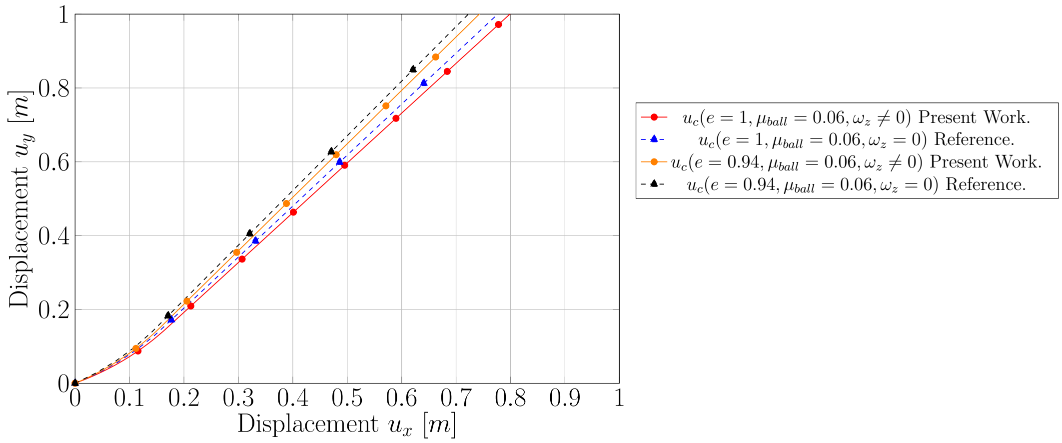

(b) Trajectory of the cue ball after impact considering spin motion.

Figure 6: Numerical vs. analytical solutions when friction between balls is considered and e_N is different to 1.

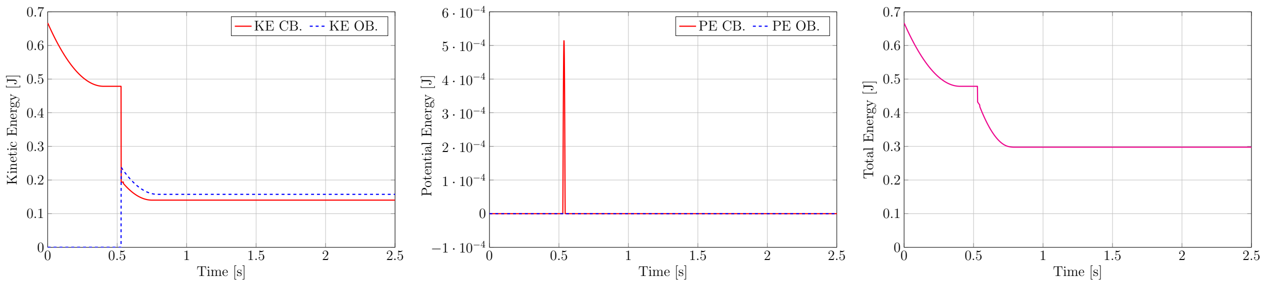

(a) Kinetic energy vs. time. (b) Potential energy vs. time. (c) Total energy vs. time.

Figure 7: Energy evolution in time for the single collision example (case $f = 0.5$, $e_N = 0.94$, $\mu_{ball} = 0.06$, $\omega_{zOB} = \omega_{zCB} = 0$ without spin motion).

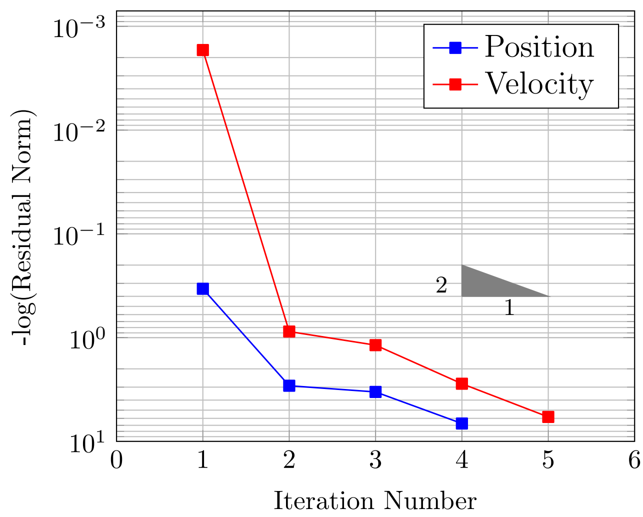

Figure 8: Evolution of logarithm of residual norm in terms of number of iterations.

5.3 Spinning Ball hitting a Ball at Rest

In this case, a spinning cue ball (CB) hitting an object ball (OB) at rest is considered. Throw effects are produced because of the spinning motion and the friction between balls. Figure 10 shows a scheme of the kinematics of impact between the CB and the OB. The CB has a spinning angular velocity ω_{zCB} and an initial linear shot velocity $\boldsymbol{v}^-$. After impact, the OB exits with a throw angle θ_{throw} and gets a post-impact velocity $\boldsymbol{v}^+$. The throw angle depends on the speed of the shot $\boldsymbol{v}^-$, the cut angle ϕ, the amount and direction of the CB spin velocity ω_{zCB}, the friction coefficient between balls μ_b and the radius R of the balls. The analytical expression to calculate θ_{throw} is given in [7]

$$\theta_{\text{throw}} = \tan^{-1}\left[\min\left(\frac{\mu_b v^- \cos\phi}{v_{rel}}, 1/7\right)\frac{v^- \sin\phi - R\omega_{zCB}}{v^- \cos\phi}\right] \tag{50}$$

where $v_{\text{rel}} = \sqrt{(v^- \sin\phi - R\omega_{zCB})^2 + (R\omega_{xCB}\cos\phi)^2}$ is the tangential component of the relative velocity between balls at the impact point, with ω_{xCB} the rolling angular velocity of the CB. Several experiments performed by Jewett [39] and Alciatore [5, 6] verified the validity of Eq.(50). The friction coefficient was computed by a fitting process from experimental data, in terms of the relative velocity of the balls at the point of impact, giving [7]:

$$\mu_b = 9.951 \times 10^{-3} + 0.108 e^{-1.088 v_{rel}} \tag{51}$$

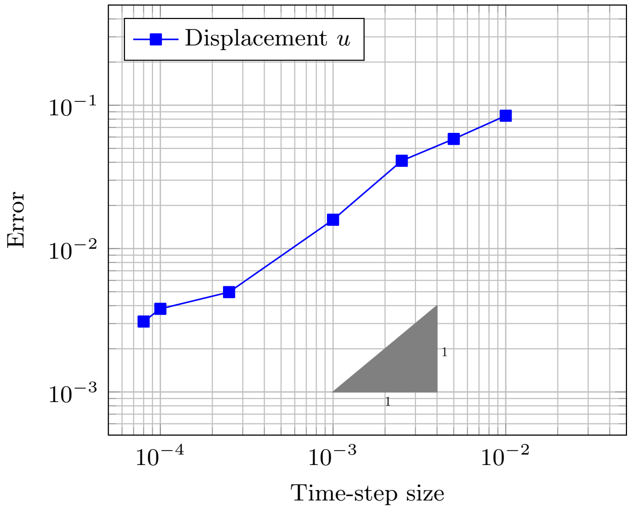

Figure 9: Convergence rate for the single collision example.

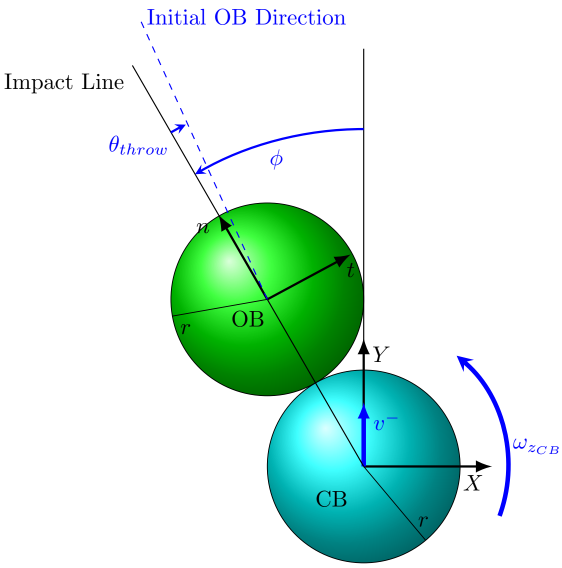

Figure 10: Throw angle effect in two spherical bodies.

Numerical experiments were performed for typical dimensions of billiard balls taken from bibliography [7], the radius of the balls are $r = 2.8575$ cm, the mass $m = 0.17$ kg and the acceleration of gravity is $g = 9.8$ m/s^2. The coefficient of friction between the balls and the cloth was neglected in order to consider only the spin impulsion which is transferred from the CB to the OB. The friction coefficient between balls was calculated as in Eq. (51). The normal restitution coefficient value between the balls, is $e_N = 1$, and between the balls and the cloth, is $e_N = 0$. The tangential restitution coefficient is $e_T = 0$ for all contact points. The CB velocity was $v^- = 1.341$ m/s (3 mph) in the x direction, thus, the angular velocity in pure rolling is $\omega_{roll} = v^-/R = 46.929$ rad/s.

Seven cases for different values of the ratio $R\omega_{zCB}/v^-$ of the CB were considered:

$$R\omega_{zCB}/v^- = [-1.25,\ -0.9,\ -0.4,\ 0,\ 0.4,\ 0.9,\ 1.25] \tag{52}$$

Simulations were performed for two values of rolling angular velocities and two values of cut angles [7]: $\omega_{xCB} = [0,\ 0.5 \times \omega_{roll}]$ (pure sliding and half sliding) and $\phi = [0,\ 30°]$ (straight impact and 30° impact).

The numerical solutions were computed with a time step $h = 1 \times 10^{-4}$ s and the total time for the simulation was 1 s. The spectral radius of the integrator was $\rho_\infty = 0.8$.

Figures 11a-b show comparisons between the throw angle θ_{throw} as a function of the ratio $R\omega_z/v^-$ calculated with Eq.(50) and the numerical solution computed with the methodology presented in this work. As Fig. 11 shows, both solutions are in a good agreement.

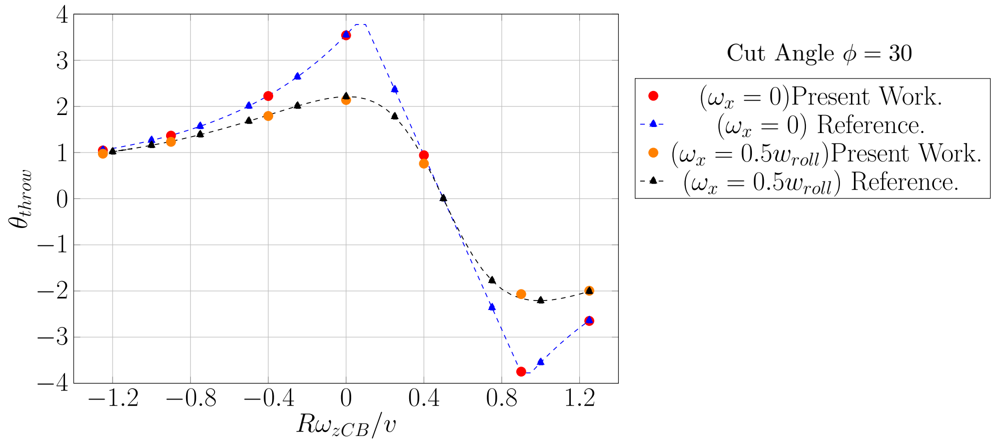

(a) Throw angle for different angular velocities with cut angle equal 30º.

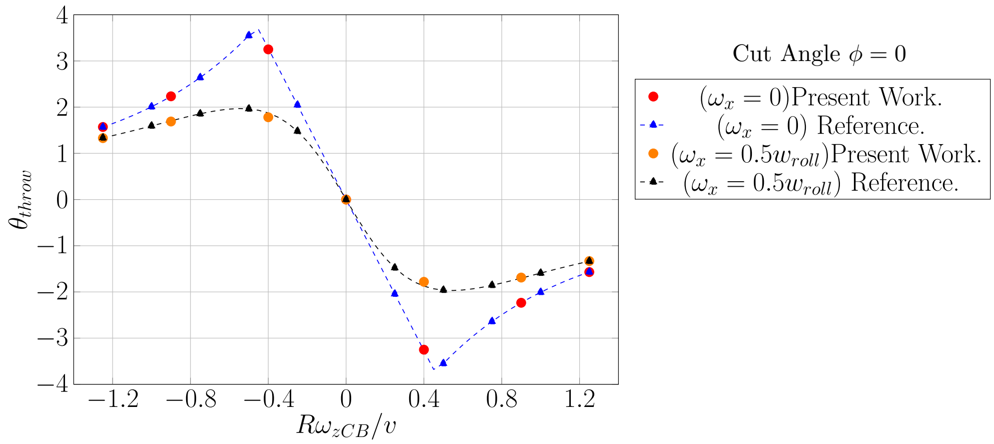

(b) Throw angle for different angular velocities with cut angle equal 0º.

Figure 11: Throw angle vs. spin angular velocity.

The displayed energy evolution is such that the system does not generate spurious energy throughout the simulation, as displayed in Figure 12. Energy is practically conserved all along the simulation, unless at the time instant of impact where an exchange of energies between balls is produced with some amount of dissipation because of friction.

The nonlinear problem at each time step was solved by Newton iteration, where the value of tolerance for convergence was $\text{tol}_r = 1 \times 10^{-5}$. The maximum number of iterations per time-step was 1, 3 and 6 for the smooth, position and velocity sub-problems, respectively. The mean number of iterations was 1 per time-step for each sub-problem. Figure 13 illustrates the evolution of the logarithm of the residual norm vs. iterations, for the case $\mu = 0$, $e_N = 1$, $\mu_{ball} = 0.06$, $\phi = 30°$, $\omega_{xCB} = 0.5 \times \omega_{roll} = 23.46$ rad/s, $v^- = 1.341$ m/s at the step of impact for which the position and velocity iterations were activated. At impact instant, a quadratic convergence rate of the Newton iterations is evidenced. No line search iterations were required

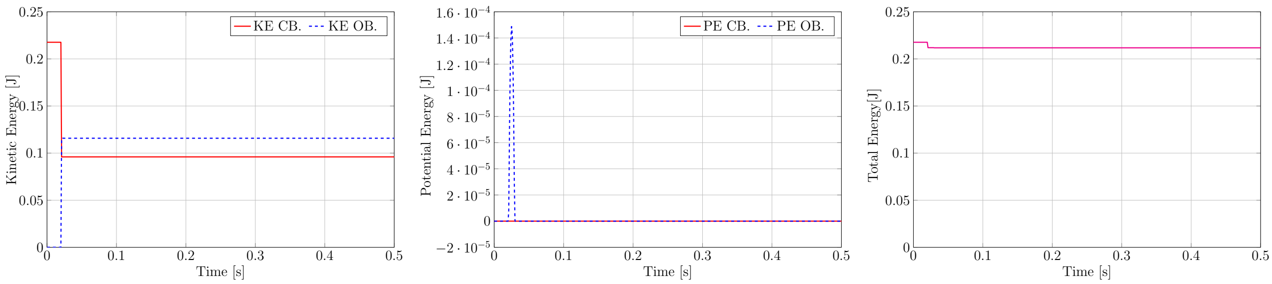

(a) Kinetic energy vs. time. (b) Potential energy vs. time. (c) Total energy vs. time.

Figure 12: Evolution of energies in time (case $\mu = 0$, $e_N = 1$, $\mu_{ball} = 0.06$, $\phi = 30°$, $\omega_{xCB} = 0.5 \times \omega_{roll} = 23.46$ rad/s, $v^- = 1.341$ m/s, $R\omega_{zCB}/v^- = 0.9$).

to achieve convergence of the Newton scheme.

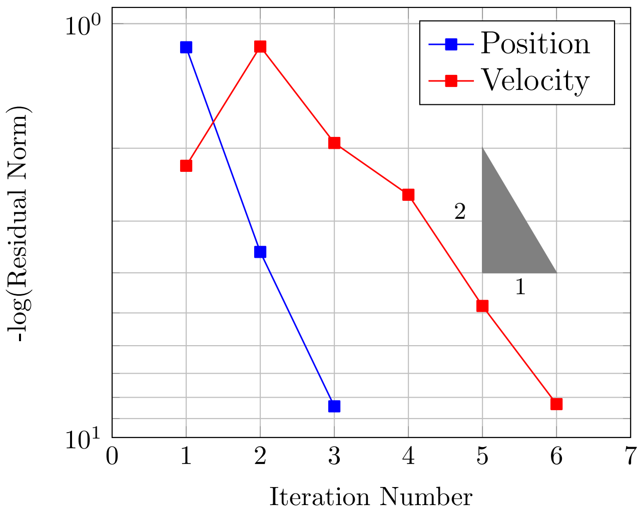

Figure 13: Evolution of the logarithm of the residual norm in terms of number of iterations.

Finally, the convergence rate with respect to the analytical solution as a function of the time step is given. The following parameters were used: $R\omega_z/v^- = -0.4$, $\omega_x = 0.5\omega_{roll}$ and $\phi = 30°$. Figure 14 shows a linear convergence as expected.

5.4 Multiple Impacts Collision

The fourth example consists of the multiple impacts collision of three spheres, see Fig. 15. Sphere 1 has an initial velocity $v_0 = 2$ m/s in the X direction, a zero initial angular velocity and is located such that contact with sphere 2 is at a distance of 0.5534 m. Spheres 2 and 3 are initially at rest and in contact. Dimensions, friction coefficients and mass properties of the balls correspond to typical values in a pool game. Each sphere is assumed rigid with a radius of 0.0283 m, mass 0.185 kg and a mass inertia moment of 0.000057 kg m^2. The normal and tangential restitution coefficients between the spheres are $e_N = 1$ and $e_T = 0$, respectively; meanwhile, $e_N = e_T = 0$ are used for the the contact between the balls and the cloth. The numerical solutions were computed with a time step $h = 1 \times 10^{-3}$ s and the total time for the simulation was 1 s. The spectral radius of the integrator was $\rho_\infty = 0.8$. The value of tolerance for convergence was $\text{tol}_r = 1 \times 10^{-5}$. Two different cases are simulated for comparison. The

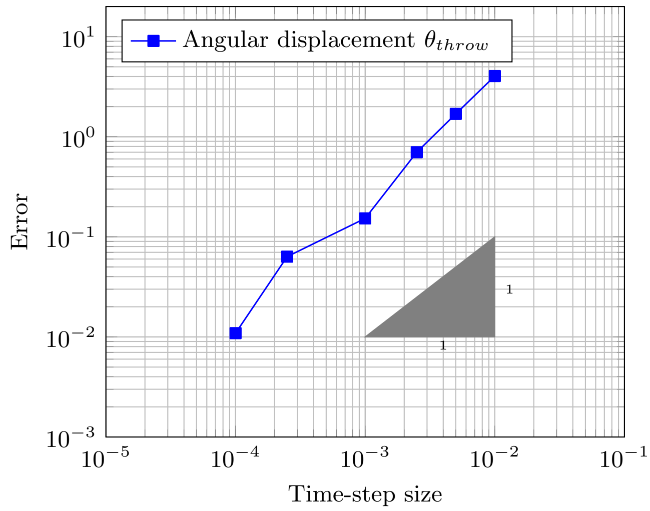

Figure 14: Convergence rate for the throw angle example with friction.

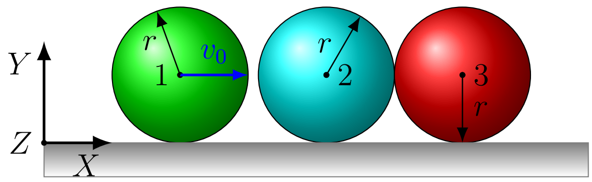

Figure 15: Multiple impacts collision of three balls.

first one is frictionless and is solved using the algorithm proposed by Cosimo *et al* [19]; in the second one, friction is considered in all contact points using the equations presented in Sec. 3.2, with friction coefficients $\mu_b = 0.06$ between balls, and $\mu = 0.2$ between balls and cloth. These values are taken from reference [7].

Let us analyze first the frictionless case. The first sphere impacts sphere 2 at 0.277 s (Fig. 16-a-b). Then, sphere 2 fully transmits its impulse to sphere 3 in only one time step. After that, sphere 3 gets the same velocity of sphere 1 before the impact, as Fig. 16-b shows. Note that spheres 1 and 2 remain at rest after impact in agreement with the experimental observations. The maximum number of iterations at smooth, position and velocity levels are 1,3 and 1, while the mean number of iterations for the three sub-problems is 1.

The complexity of the problem is increased when friction is taken into account; for this reason, the global convergence rate of the contact algorithms is somehow deteriorated. The initial conditions, the masses, the dimensions and solver parameters are the same as in the case before. At the beginning of motion, the angular velocity of the sphere 1 decreases linearly in time reflecting that it is in sliding movement until time 0.284 s; then, the angular velocity becomes constant, which expresses that it changes to a pure rolling movement, see Fig.17-b-c. The first impact is produced at time 0.328 s, when the spheres 2 and 3 are moved forward, see Fig. 17-a. However, the sphere 1 bounces back, see the detail of Fig. 17-b where the velocity is negative. The detail of Fig. 17-d shows the height of rebound of the spheres 1 and 3 after the first impact. When compared with the frictionless case, we remark that there is a delay as a consequence of friction between the sphere and the plane, as depicted in Fig. 17-a-b-c.

After the bounce and once that sphere 1 touches the plane again, due to the rolling movement it impacts again sphere 2. Then, there is a sequence of impacts between spheres 1 and 2 that goes on with decreasing intensity and with frictional sliding in sphere 1 and pure rolling in

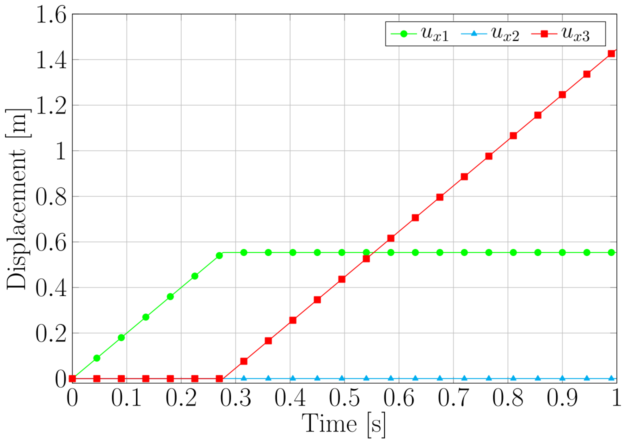

(a) Displacement vs. time.

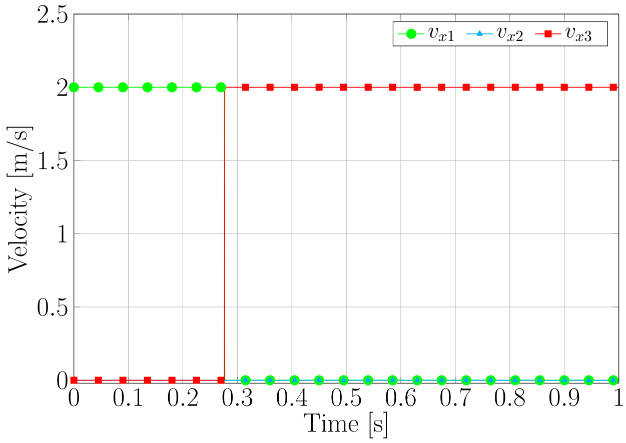

(b) Velocity vs. time.

Figure 16: Frictionless case. Displacement and velocity of the spheres.

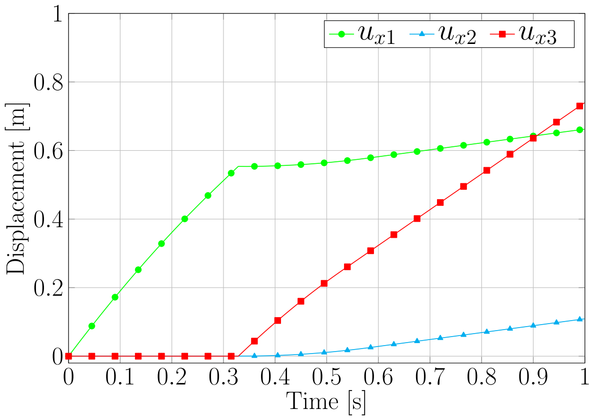

(a) Horizontal displacement vs. time.

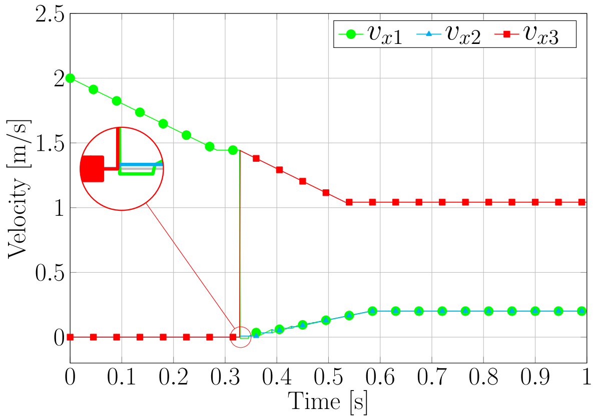

(b) Velocity vs. time.

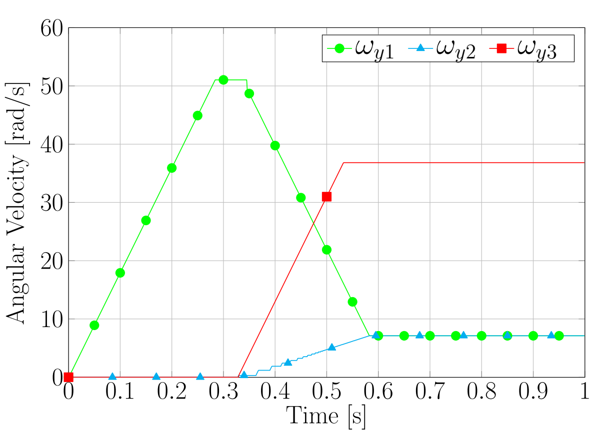

(c) Angular velocity vs. time.

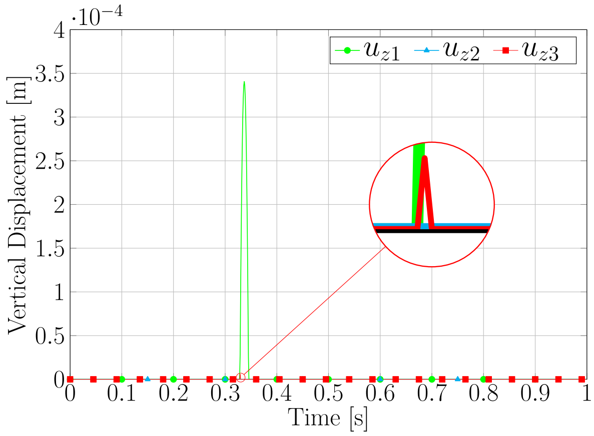

(d) Vertical displacement vs. time.

Figure 17: Frictional case. Displacements and velocities of the spheres.

sphere 2, see Fig. 17-b. Finally, both spheres move forward together with a rolling movement and without impacts, see Fig. 17-c. On the other hand, sphere 3 moves forward with sliding movement reducing the velocity until reaching pure rolling.

In this example, the maximum number of iterations at smooth, position and velocity levels are 1,4 and 2, while the mean number of iterations for the three sub-problems is 1. No line search iterations were required to achieve convergence of the Newton scheme.

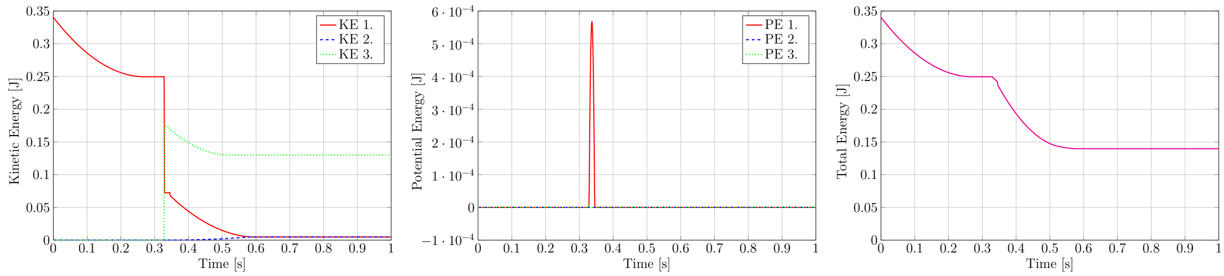

(a) Kinetic Energy vs. time. (b) Potential Energy vs. time. (c) Total Energy vs. time.

Figure 18: Evolution of energies in time, frictional case.

Figure 18-a shows that initially, the cue ball is in sliding movement with a reduction of kinetic energy. Subsequently, it enters in pure rolling motion conserving energy until collision with the second ball. At the moment of impact, the cue ball rebounds and separates from ground, as illustrated in Fig. 18-b, where an increase in potential energy is observed. Most of kinetic energy is transferred to ball 3, and the balls change progressively from sliding to pure rolling motion reducing the total kinetic energy, as shown in Fig. 18-c. Finally ball 3 moves in pure rolling movement without losing energy, while balls 1 and 2 are almost stopped.

Finally, the convergence rate as a function of the time step is given. The error was calculated with respect to a numerical solution with time step $h = 1 \times 10^{-5}$ s. Figure 19 shows a linear convergence as expected.

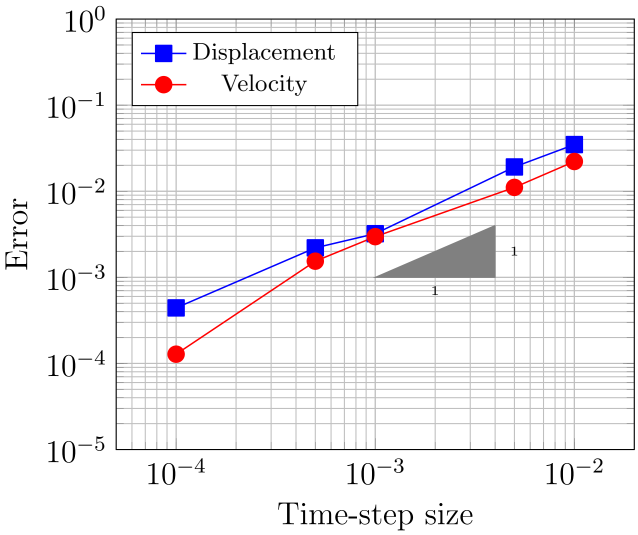

Figure 19: Convergence analysis for the multiple impact example with friction.

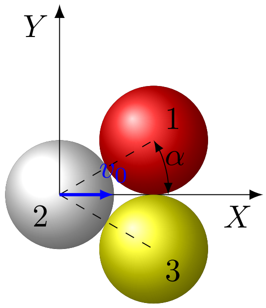

Figure 20: The Bernoulli problem.

5.5 Bernoulli Problem

This example, proposed by Liu *et al.* [46], consists of a frictionless multiple impacts collision involving three rigid spheres in contact with each other at the initial configuration as shown in Figure 20. Sphere 2 initially has a velocity of $v_0 = 1$ m/s in the X direction and zero initial angular velocity. Meanwhile, spheres 1 and 3 are at rest. The three balls have radius $r = 1$ m, mass $m = 1$ kg, and moment of inertia of 0.4 kg m^2. The normal and tangential restitution coefficients between the spheres are $e_N = 1$ and $e_T = 0$, respectively, and between spheres and plane they are $e_N = e_T = 1$. The results are compared with the analytical solution:

$$\begin{aligned} v_{x1} &= v_{x3} = \frac{2v_0}{3+\tan^2\alpha} & \qquad v_{x2} &= v_0 - \frac{4v_0}{3+\tan^2\alpha} \\ v_{y1} &= -v_{y3} = \frac{2v_0\tan\alpha}{3+\tan^2\alpha} & \qquad v_{y2} &= 0 \end{aligned} \tag{53}$$

The numerical solution was computed with a time step $h = 1\times10^{-2}$ s and the total time for the simulation was 0.6 s. The spectral radius of the integrator was $\rho_\infty = 0.8$. The value of tolerance for convergence was $\mathrm{tol}_r = 1\times10^{-5}$. The maximum number of iterations for the smooth, position, and velocity levels were 1, 3 and 1, and the mean number of iterations for the three sub-problems was 1. No line search iterations were required to achieve convergence of the Newton scheme.

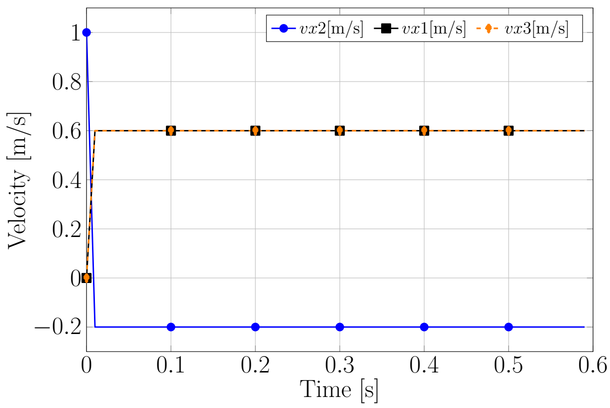

(a) Velocity Vx vs. time.

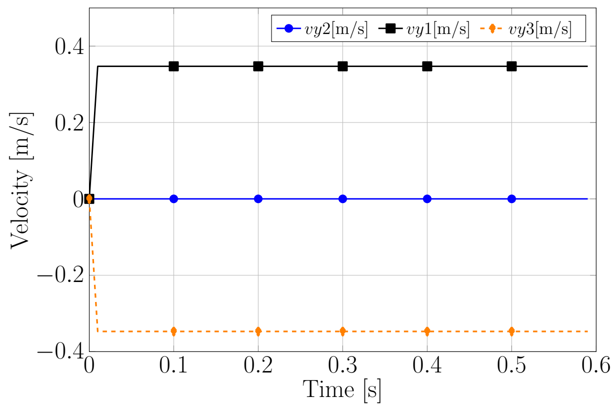

(b) Velocity Vy vs. time.

Figure 21: Velocity of the balls.

Figure 21 shows the computed velocities vs. time for each ball. The values of the velocities after impact are in good agreement with those calculated by the analytical solution (53), which

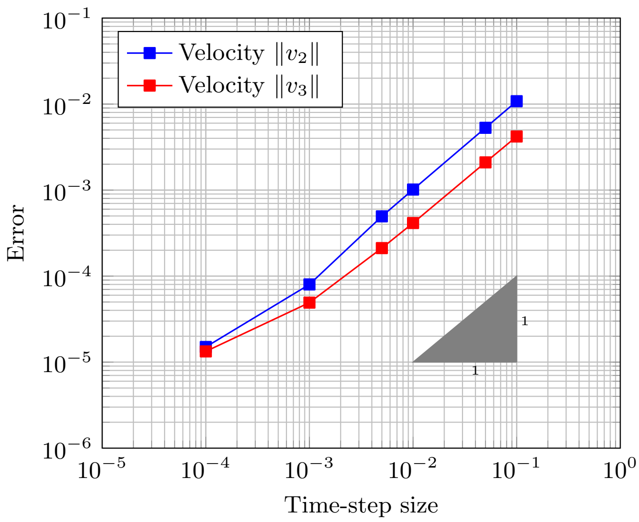

Figure 22: Convergence analysis for the Bernoulli problem.

predicted $v_{x1} = v_{x3} = 0.6$ m/s, $v_{x2} = -0.2$ m/s, $v_{y1} = -v_{y3} = 0.3464$ m/s and $v_{y2} = 0$ m/s. Finally, Fig. 22 shows the convergence rate of the velocity modulus of balls 2 and 3 compared with the analytical solutions given by Eqs. (53), which is linear, as expected.

5.6 Billiard balls interaction

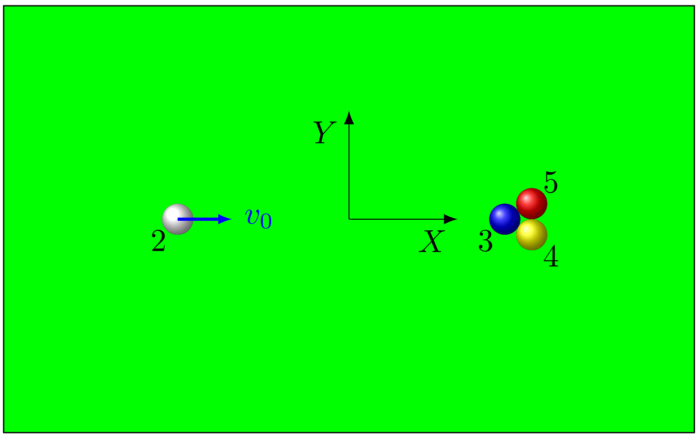

Figure 23: Billiard break configuration.

This problem consists of a typical billiard break, see Figure 23. It was initially presented by Gismeros *et al.* [18] in the frame of the penalty based-approach. The example allows us to study the ability of the algorithm to solve problems with multiple impacts, with the possibility to consider rolling friction effects. The results with those of reference [18], in which a penalty approach was used to model impacts, were compared.

The four balls have a radius $r = 0.028575$ m, a weight $mg = 1.666$ N and an inertia $I = 0.000055$ kg m^2. The table has a length of 2.54 m and a width of 1.27 m. The values of the friction coefficient μ and the normal restitution coefficient e_N are 0.2 and 0, respectively, for the contact between the balls and the table. The coefficients of friction and restitution for the contact between balls are $\mu_b = 0.06$ and $e_N = 0.93$, respectively. The contact between the balls and the edges of the table are represented with friction and restitution coefficients $\mu = 0$ and $e_N = 0.85$, respectively. The tangential restitution coefficient was set to $e_T = 0$ in all contacts. The white ball, labeled 2, starts motion with a speed of $v_x = 10.729$ m/s and hits the three balls labeled 3, 4 and 5, that are in contact between them and at rest (see Fig. 23).

In this work two cases are analyzed: in the first one, the rolling resistance between the spheres and the plane is neglected, while in the second one a rolling resistance radius $\rho = 0.005$ m is adopted. In both cases, the total simulation time was 3 s with a time step of 1×10^{-3} s and the value of tolerance for convergence was $\text{tol}_r = 1 \times 10^{-5}$. In the first case, the cue ball starts with a velocity of 10.729 m/s and null rolling velocity, and impacts the balls at a slightly lower velocity due to the sliding friction between the ball and the plane, see Fig. 24-a. After multiple impacts, ball 3 moves forward with a low velocity. As it can be seen, once the balls are in pure rolling, their velocity remains constant, see Fig. 24-a. The second case is similar to the first; however, the balls reach the rest condition due to the action of the rolling resistance, see Fig. 24-b. Figure 25-a shows the linear and the angular velocity of ball

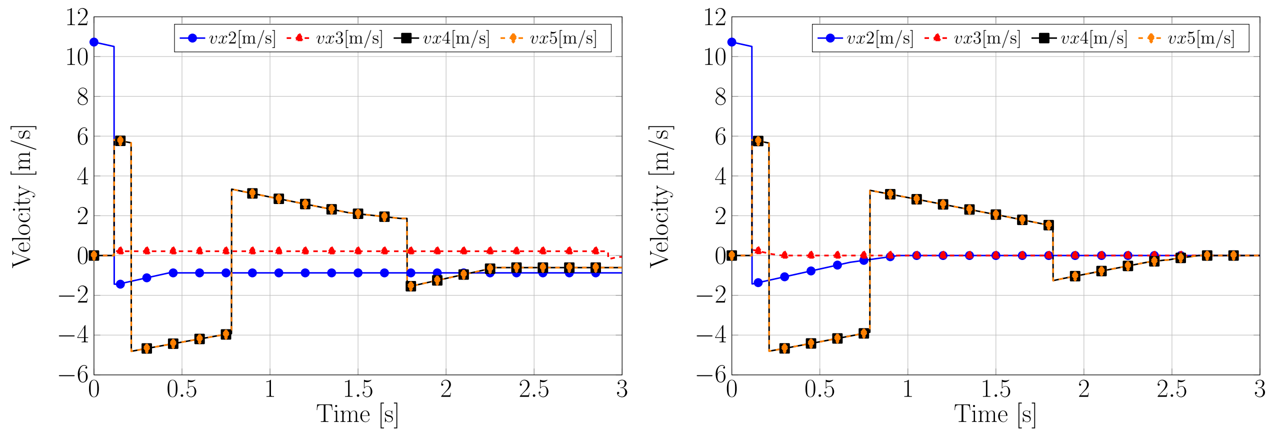

(a) With sliding friction.

(b) With sliding and rolling friction.

Figure 24: Computed velocities in the billiard break problem.

2. After the multiple impact at time 0.114 s, a small discrepancy is observed compared to the reference results. In the numerical solutions presented with the present methodology, ball 2 jumps vertically after impact, see Fig. 25-b. Then, the angular velocity remains constant in the period of time that the ball is in the air, see Fig. 25-a. Then, once ball 2 comes into contact with the plane, it begins to slide backwards until finally becomes a pure rolling movement. The proposed methodology does not present any penetration between bodies in contact, as occurs in penalty-based approaches, and the computation time was reduced from 25000 s, as required by the methodology of the reference work, to just 40 s. The maximum number of iterations for the smooth, position, and velocity levels were 1, 7 and 4 (frictional case). The mean number of iterations was 1,2 and 1 for the smooth, position, and velocity levels, respectively. At first impact instant, in the third and fourth iteration of the Newton method, 9 and 26 iterations of line search at position level were required to convergence, respectively. In the remaining time steps, no line search iterations were required to achieve the convergence of the Newton scheme. The quadratic convergence rate of the Newton iterations is shown in Fig. 26

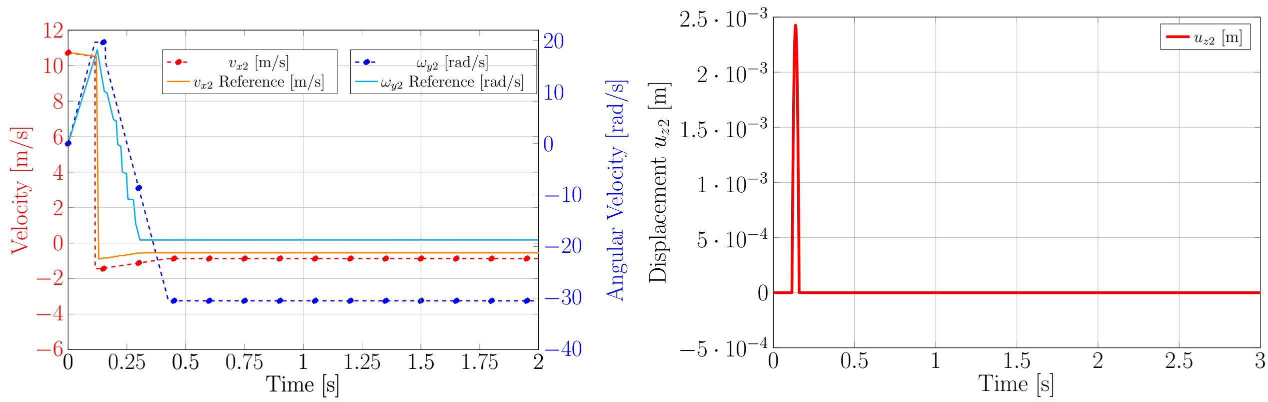

(a) Comparison of the velocity and angular velocity of the white ball.

(b) Vertical displacement of white ball vs. time.

Figure 25: Comparison with penalty-based approach in the billiard break problem.

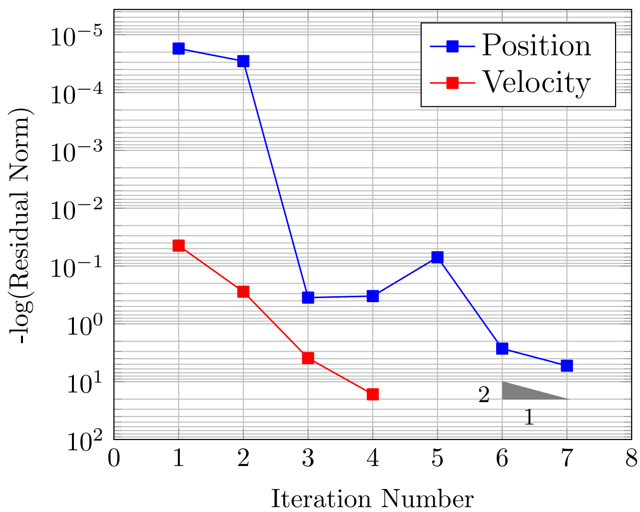

Figure 26: Evolution of the logarithm of the residual norm in terms of number of iterations.

6 Conclusions

A new frictional contact element to simulate the impact between spherical rigid bodies is presented. The paper gives a detailed kinematic formulation using large rotations and absolute coordinates, with explicit expressions of internal forces and Hessians.

In addition, a new methodology for handling simultaneous multiple impacts with friction effects is given. The algorithm is based on the frictionless proposal by Cosimo *et al.* [19], here modified to consider friction terms, and in which the Newton impact law is sequentially applied by assuming instantaneous local impact times. The strategy has the advantage that it does not require any intervention of the user or any topological analysis for defining the sequence for processing the multiple impacts.

The studied examples demonstrate that the proposed methodology keeps a low computational cost compared with the classical smooth continuous approaches. Results were compared with results of other authors, either analytical or experimentally validated, with excellent convergence rate to the solution.

This approach may also be advantageous when describing the general case of flexible multibody systems. The extension from rigid multibody dynamics to the FEM (finite element method) context can be done in a very consistent manner avoiding rewriting the equations for each particular case.

Acknowledgements

This work received financial support from Consejo Nacional de Investigaciones Cient´ıficas y Técnicas (CONICET) PIP11220200101688CO and Universidad Tecnológica Nacional PID-UTN AMECAFE0008102TC which are gratefully acknowledged.

References

[1] V. Acary. Higher order event capturing time-stepping schemes for nonsmooth multibody systems with unilateral constraints and impact. *Applied Numerical Mathematics*, 62:1259–1275, 2012.

[2] V. Acary. Projected event-capturing time-stepping schemes for nonsmooth mechanical systems with unilateral contact and Coulomb's friction. *Computer Methods in Applied Mechanics and Engineering*, 256:224–250, apr 2013.

[3] V. Acary and F. Bourrier. Coulomb friction with rolling resistance as a cone complementarity problem. *European Journal of Mechanics - A/Solids*, 85:104046, 2021.

[4] P. Alart and A. Curnier. A mixed formulation for frictional contact problems prone to Newton like solution methods. *Computer Methods in Applied Mechanics Engeenering*, 92(3):353–375, 1991.

[5] D.G. Alciatore. Throw - Part II: follow and draw effects, Dr. Dave's illustrated principles. *Billiards Digest*, 29(10), 2006.

[6] D.G. Alciatore. Throw - Part III: follow and draw effects, Dr. Dave's illustrated principles. *Billiards Digest*, 29(11), 2006.

[7] D.G. Alciatore. *The Illustrated Principles of Pool and Billiards*. Sterling, first edition edition, 2017.

[8] A. Bosten and O. Brüls. On the evaluation of the tangential slip increment in quasi-static beam-to-beam contact problems. In *ECCOMAS Thematic Conference and IACM Special Interest Conference Highly Flexible Slender Structures (HFSS 2023)*, page 1. University of Rijeka, 2023.

[9] A. Bowling, D. Flickinger, and S. Harmeyer. Energetically consistent simulation of simultaneous impacts and contacts in multibody systems with friction. *Multibody System Dynamics*, 22(1):27–45, 2009.

[10] B. Brogliato. *Nonsmooth Mechanics*. Springer International Publishing, 2016.

[11] B. Brogliato, H. Zhang, and C. Liu. Analysis of a generalized kinematic impact law for multibody-multicontact systems, with application to the planar rocking block and chains of balls. *Multibody System Dynamics*, 27(3):351–382, 2012.

[12] O. Brüls, V. Acary, and A. Cardona. Simultaneous enforcement of constraints at position and velocity levels in the nonsmooth generalized-α scheme. *Computer Methods in Applied Mechanics and Engineering*, 281:131–161, 2014.

[13] Olivier Brüls, Vincent Acary, and Alberto Cardona. *On the Constraints Formulation in the Nonsmooth Generalized-alpha Method*, pages 335–374. Springer International Publishing, Cham, 2018.

[14] G. Capobianco, J. Harsch, S.R. Eugster, and R.I. Leine. A nonsmooth generalized-alpha method for mechanical systems with frictional contact. *International Journal for Numerical Methods in Engineering*, 122(22):6497–6526, 2021.

[15] A. Cardona, I. Klapka, and M. Géradin. Design of a new finite element programming environment. *Engineering Computations*, 11:365–381, 1994.

[16] R. Carretero-González, D. Khatri, M.A. Porter, P.G. Kevrekidis, and C. Daraio. Dissipative solitary waves in granular crystals. *Physical review letters*, 102(2):024102, 2009.

[17] Q-z. Chen, V. Acary, G. Virlez, and O. Brüls. A nonsmooth generalized-α scheme for flexible multibody systems with unilateral constraints. *International Journal for Numerical Methods in Engineering*, 96:487–511, 2013.

[18] E. Corral, R. Gismeros, F. Marques, P. Flores, M.J. Gómez Garcia, and C. Castejón. Dynamic modeling and analysis of pool balls interaction. In *Multibody Dynamics 2019: Proceedings of the 9th ECCOMAS Thematic Conference on Multibody Dynamics*, pages 79–86. Springer, 2020.

[19] A. Cosimo, F.J. Cavalieri, A. Cardona, and O. Brüls. On the adaptation of local impact laws for multiple impact problems. *Nonlinear Dynamics*, 102(4):1997–2016, 2020.

[20] A. Cosimo, J. Galvez, F.J. Cavalieri, A. Cardona, and O. Brüls. A robust nonsmooth generalized-α scheme for flexible systems with impacts. *Multibody System Dynamics*, 48(2):127–149, 2020.

[21] Y. Cuneyt, M. Gharib, and Y. Hurmuzlu. Solving frictionless rocking block problems with multiple impacts. *Proceeding of the Royal Society A: Mathematical, Physical and Engineering Science*, 465:3323–3339, 2009.

[22] G. Darboux. Étude géométrique sur les percussions et le choc des corps. *Bulletin des Sciences Mathématiques et Astronomiques*, 4(1):126–160, 1880.

[23] G. De Saxcé and Z.-Q. Feng. The bipotential method: a constructive approach to design the complete contact law with friction and improved numerical algorithms. *Mathematical and computer modelling*, 28(4-8):225–245, 1998.

[24] G. De Saxcé and Z.Q. Feng. New inequality and functional for contact with friction: The implicit standard material approach. *Mechanics of Structures and Machines*, 19(3):301–325, 1991.

[25] D.M. Flickinger and A. Bowling. Simultaneous oblique impacts and contacts in multibody systems with friction. *Multibody System Dynamics*, 23:249–261, 2010.

[26] P. Flores, M. Machado, M.T. Silva, and J.M. Martins. On the continuous contact force models for soft materials in multibody dynamics. *Multibody System Dynamics*, 25(3):357–375, 2011.

[27] M. Frémond. Rigid bodies collisions. *Physics Letters A*, 204(1):33 – 41, 1995.

[28] J. Galvez, F.J. Cavalieri, A. Cosimo, O. Brüls, and A. Cardona. A nonsmooth frictional contact formulation for multibody system dynamics. *International Journal for Numerical Methods in Engineering*, 121(16):3584–3609, 2020.

[29] M. Gharib, A. Celik, and Y. Hurmuzlu. Shock absorption using linear particle chains with multiple impacts. *ASME Journal of Applied Mechanics*, 78(031005), 2011.

[30] C. Glocker. Energetic consistency conditions for standard impacts. *Multibody System Dynamics*, 29(1):77–117, 2013.

[31] C. Glocker and U. Aeberhard. The geometry of Newton's cradle. In *Advances in Mechanics and Mathematics*, pages 185–194.

[32] C. Glocker and F. Pfeiffer. Multiple impacts with friction in rigid multibody systems. *Nonlinear Dynamics*, 7(4):471–497, 1995.

[33] Christoph Glocker. *An Introduction to Impacts*, pages 45–101. Springer Vienna, Vienna, 2006.

[34] M. Géradin and A. Cardona. *Flexible Multibody Dynamics: A Finite Element Approach*. Wiley, 2001.

[35] I. Han and B.J. Gilmore. Multi-body impact motion with friction analysis, simulation, and experimental validation. *Journal of Mechanical Design*, 115(3):412, 1993.

[36] G. Hu, Z. Hu, B. Jian, L. Liu, and H. Wan. On the determination of the damping coefficient of non-linear spring-dashpot system to model Hertz contact for simulation by discrete element method. *Journal of Computers*, 6:984–988, 2011.

[37] J. Huang, M. Vicente da Silva, and K. Krabbenhoft. Three-dimensional granular contact dynamics with rolling resistance. *Computers and Geotechnics*, 49:289 – 298, 2013.

[38] K.H. Hunt and F.R.E. Crossley. Coefficient of restitution interpreted as damping in vibroimpact. *J. Appl. Mech*, 42(2):440–445, 1975.

[39] B. Jewett. Seeking truth of beliefs. Technical report, Tech Talk, Billiards Digest, 1995.

[40] Stéphane Job, Francisco Melo, Adam Sokolow, and Surajit Sen. How hertzian solitary waves interact with boundaries in a 1d granular medium. *Physical review letters*, 94(17):178002, 2005.

[41] H.M. Lankarani and P.E. Nikravesh. A contact force model with hysteresis damping for impact analysis of multibody systems. *Journal of Mechanical Design*, 112(3):369–376, 1990.

[42] R.I. Leine, D.H. van Campen, and C. Glocker. Nonlinear dynamics and modeling of various wooden toys with impact and friction. *Journal of Vibration and Control*, 9:25–78, 2003.

[43] R.I. Leine and N van de Wouw, editors. *Stability and Convergence of Mechanical Systems with Unilateral Constraints*. Springer Berlin Heidelberg, 2008.

[44] R.I. Leine and N. van de Wouw. Stability properties of equilibrium sets of non-linear mechanical systems with dry friction and impact. *Nonlinear Dynamics*, 51(4):551–583, 2008.

[45] C. Liu, Z. Zhao, and B. Brogliato. Frictionless multiple impacts in multibody systems. I. Theoretical framework. *Proceedings of the Royal Society A: Mathematical, Physical and Engineering Sciences*, 464(2100):3193–3211, 2008.

[46] C. Liu, Z. Zhao, and B. Brogliato. Frictionless multiple impacts in multibody systems. II. Numerical algorithm and simulation results. *Proceedings of the Royal Society A: Mathematical, Physical and Engineering Sciences*, 465(2101):1–23, 2009.

[47] J. J. Moreau. Unilateral contact and dry friction in finite freedom dynamics. In *Nonsmooth Mechanics and Applications*, pages 1–82. Springer Vienna, 1988.

[48] J.J. Moreau. Some numerical methods in multibody dynamics: application to granular materials. *European Journal of Mechanics-A/Solids*, 13(4-suppl):93–114, 1994.

[49] J.J. Moreau. Numerical aspects of the sweeping process. *Computer Methods in Applied Mechanics and Engineering*, 177(3-4):329–349, jul 1999.

[50] I. Newton. *Philosophiae Naturalis Principia Mathematica.* Reg. Soc. Phreases, 1686.

[51] N.S. Nguyen and B. Brogliato. *Multiple impacts in dissipative granular chains*, volume 72. Springer Science & Business Media, 2013.

[52] F. Pfeiffer. Multibody systems with unilateral constraints. *J. Appl. Maths. Mechs.*, 65(4):665–670, 2001.

[53] F. Pfeiffer. Energy considerations for frictional impacts. *Archive of Applied Mechanics*, 80(1):47–56, 2010.

[54] F. Pfeiffer and C. Glocker. *Multibody Dynamics with Unilateral Contacts.* Wiley-VCH Verlag GmbH, aug 1996.

[55] S.D. Poisson. *Traité de Meécanique.* Bachelier, second edition edition, 1833.

[56] M. Rodrigues da Silva, F. Marques, M. Tavares da Silva, and P. Flores. A compendium of contact force models inspired by Hunt and Crossley's cornerstone work. *Mechanism and Machine Theory*, 167:104501, 2022.

[57] T. Schindler and V. Acary. Timestepping schemes for nonsmooth dynamics based on discontinuous galerkin methods: definition and outlook. *Mathematics and Computers in Simulation*, 95:180–199, 2014.

[58] D.E. Stewart and J.C. Trinkle. An implicit time-stepping scheme for rigid body dynamics with inelastic collisions and Coulomb friction. *Int. J. for Numerical Methods in Engineering*, 39(15):2673–2691, 1996.

[59] C. Studer. *Numerics of Unilateral Contacts and Friction: Modeling and Numerical Time Integration in Non-smooth Dynamics. Lecture Notes in Applied and Computational Mechanics*, volume 47. Springer, 2009.

[60] E. Sánchez, A Cosimo, O. Brüls, A. Cardona, and F.J Cavalieri. Non-smooth numerical solution for Coulomb friction and sliding, rolling and spinning resistance of spheres applied to flexible multibody system dynamics. *Multibody System Dynamics*, 20(20):20–20, 2023.

[61] A. Tasora and M. Anitescu. A complementarity-based rolling friction model for rigid contacts. *Meccanica*, 48(7):1643–1659, 2013.

[62] R.E. Wallace and M.C. Schroeder. Analysis of billiard ball collisions in two dimensions. *American Journal of Physics*, 56(9), 1988.

[63] A.S. Yigit, A.G. Ulsoy, and R.A. Scott. Spring-dashpot models for the dynamics of a radially rotating beam with impact. *Journal of sound and Vibration*, 142(3):515–525, 1990.

[64] H. Zhang, B. Brogliato, and C. Liu. Dynamics of planar rocking-blocks with Coulomb friction and unilateral constraints: Comparisons between experimental and numerical data. *Multibody System Dynamics*, 2013.

[65] H. Zhang, B. Brogliato, and C. Liu. Study of the planar rocking-block dynamics with Coulomb friction: Critical kinetic angles. *ASME Journal of Computational and Nonlinear Dynamics*, 8(3):021002, 2013.

[66] J. Zhang, W. Li, L. Zhao, and G. He. A continuous contact force model for impact analysis in multibody dynamics. *Mechanism and Machine Theory*, 153:103946, 2020.

[67] P. Zhao, J. Liu, Y. Li, and C. Wu. A spring-damping contact force model considering normal friction for impact analysis. *Nonlinear Dynamics*, 105:1437–1457, 2021.

Appendix A

Algorithm 1 Modified Nonsmooth GGL generalized-α time integration scheme.

Inputs: initial values $\boldsymbol{q}_0$ and $\boldsymbol{v}_0$;
Compute consistent value of $\dot{\breve{\boldsymbol{v}}}_0$
$\boldsymbol{a}_0 := \dot{\breve{\boldsymbol{v}}}_0$
for $n = 0$ to $n_{\text{final}} - 1$ **do**
    $\dot{\breve{\boldsymbol{v}}}_{n+1} := \boldsymbol{0}$, $\breve{\boldsymbol{\lambda}}^{\mathcal{U}}_{n+1} := \boldsymbol{0}$, $\boldsymbol{\nu}_{n+1} := \boldsymbol{0}$
    $\boldsymbol{\Lambda}_{n+1} := \boldsymbol{0}$, $\boldsymbol{W}_{n+1} := \boldsymbol{0}$, $\boldsymbol{U}_{n+1} := \boldsymbol{0}$
    $\boldsymbol{a}_{n+1} := 1/(1-\alpha_m)(\alpha_f \dot{\breve{\boldsymbol{v}}}_n - \alpha_m \boldsymbol{a}_n)$
    $\boldsymbol{v}_{n+1} := \breve{\boldsymbol{v}}_{n+1} := \boldsymbol{v}_n + h(1-\gamma)\boldsymbol{a}_n + h\gamma\boldsymbol{a}_{n+1}$
    $\boldsymbol{q}_{n+1} := \boldsymbol{q}_n + h\boldsymbol{v}_n + h^2(1/2\ - \beta)\boldsymbol{a}_n + h^2\beta\boldsymbol{a}_{n+1}$
    Step 1 (smooth motion):
    for $i = 1$ to i_{max} **do**
        Compute residual $\boldsymbol{r}^s$
        if $\|\boldsymbol{r}^s\| <$ tol **then** break **end if**
        Compute the iteration matrix $\boldsymbol{S}^s_t$
        $\Delta\boldsymbol{x}^s := -(\boldsymbol{S}^s_t)^{-1}\boldsymbol{r}^s$
        $\breve{\boldsymbol{v}}_{n+1} := \breve{\boldsymbol{v}}_{n+1} + \Delta\breve{\boldsymbol{v}}$
        $\dot{\breve{\boldsymbol{v}}}_{n+1} := \dot{\breve{\boldsymbol{v}}}_{n+1} + (1-\alpha_m)/((1-\alpha_f)\gamma h)\Delta\breve{\boldsymbol{v}}$
        $\boldsymbol{q}_{n+1} := \boldsymbol{q}_{n+1} + h\beta/\gamma\Delta\breve{\boldsymbol{v}}$
        $\breve{\boldsymbol{\lambda}}^{\mathcal{U}}_{n+1} := \breve{\boldsymbol{\lambda}}^{\mathcal{U}}_{n+1} + \Delta\breve{\boldsymbol{\lambda}}^{\mathcal{U}}$
    end for
    Step 2 (projection on position constraints):
    for $i = 1$ to i_{max} **do**
        Compute residual $\boldsymbol{r}^p$
        if $||\boldsymbol{r}^p|| <$ tol **then** break **end if**
        Compute $\boldsymbol{S}^p_t$
        $\Delta\boldsymbol{x}^p := -(\boldsymbol{S}^p_t)^{-1}\boldsymbol{r}^p$
        $\boldsymbol{U}_{n+1} := \boldsymbol{U}_{n+1} + \Delta\boldsymbol{U}$
        $\boldsymbol{q}_{n+1} := \boldsymbol{q}_{n+1} + \Delta\boldsymbol{U}$
        $\boldsymbol{\nu}_{n+1} := \boldsymbol{\nu}_{n+1} + \Delta\boldsymbol{\nu}$
    end for
    Step 3 (projection on velocity constraints):
    for $i = 1$ to i_{max} **do**
        Compute residual $\boldsymbol{r}^v$
        if $||\boldsymbol{r}^v|| <$ tol **then** break **end if**
        Compute $\boldsymbol{S}^v_t$
        $\Delta\boldsymbol{x}^v := -(\boldsymbol{S}^v_t)^{-1}\boldsymbol{r}^v$
        $\boldsymbol{W}_{n+1} := \boldsymbol{W}_{n+1} + \Delta\boldsymbol{W}$
        $\boldsymbol{v}_{n+1} := \breve{\boldsymbol{v}}_{n+1} + \boldsymbol{W}_{n+1}$
        $\boldsymbol{\Lambda}_{n+1} := \boldsymbol{\Lambda}_{n+1} + \Delta\boldsymbol{\Lambda}$
    end for
    $\boldsymbol{a}_{n+1} := \boldsymbol{a}_{n+1} + (1-\alpha_f)/(1-\alpha_m)\dot{\breve{\boldsymbol{v}}}_{n+1}$
end for

Appendix B

The accuracy of Eq.(36), which gives the incremental tangential slip between balls, is studied by a simple numerical experiment. The example consists of a sphere A that rolls without slipping over a fixed sphere B following a planar motion. Figure 27-a shows the previous configuration at time t_n while Fig. 27-b shows the current configuration at time t_{n+1}. The inertia frame is located at the center of sphere B.

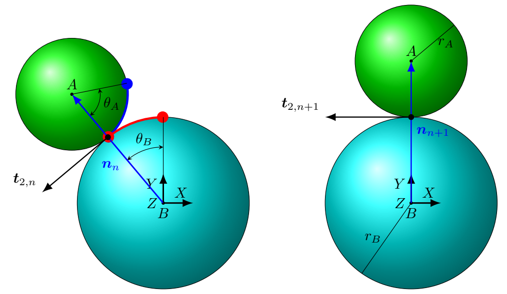

(a) Previous configuration at t_n.

(b) Current configuration at t_{n+1}

Figure 27: Rolling without slipping between two spherical bodies.

Since sphere B is fixed, the position and the rotational vectors at previous time t_n and at current time step t_{n+1} are

$$\boldsymbol{x}_{B,n+1} = \boldsymbol{x}_{B,n} = \mathbf{0} \qquad \boldsymbol{\Psi}_{B,n+1} = \boldsymbol{\Psi}_{B,n} = \mathbf{0} \tag{54}$$

The position and the rotational vectors at the current time step for sphere A are

$$\boldsymbol{x}_{A,n+1} = [0\ (r_A + r_B)\ 0]^T \qquad \boldsymbol{\Psi}_{A,n+1} = \mathbf{0} \tag{55}$$

Meanwhile, the position and rotational vectors of sphere A at the previous time step can be calculated from standard kinematic analysis as follows

$$\boldsymbol{x}_{A,n} = [-(r_A + r_B)\sin\theta_B\ (r_A + r_B)\cos\theta_B\ 0]^T \qquad \boldsymbol{\Psi}_{A,n} = [0\ 0\ \phi_A]^T \tag{56}$$

where θ_A (respectively θ_B) is the angle embracing the trajectory of the contact point over sphere A (respectively over sphere B) and where $\phi_A = \theta_A + \theta_B$ is the total angular displacement of sphere A. The rotational increment vector of sphere A from t_n to t_{n+1} is given by

$$\boldsymbol{\Psi}_{A,\text{incr}} = [0\ 0\ -\phi_A]^T \tag{57}$$

The rolling without slipping contact condition (equality of arc-lengths) is written as

$$\theta_A\, r_A = \theta_B\, r_B \tag{58}$$

Therefore, the total angular displacement of sphere A ϕ_A can be expressed as a function of angle θ_B giving,

$$\phi_A = \frac{r_A + r_B}{r_A}\,\theta_B = \left(1 + \frac{r_B}{r_A}\right)\theta_B \tag{59}$$

Besides, the tangential and normal vectors at the contact point, evaluated at the previous time step, are given by

$$\boldsymbol{t}_{2,n} = [\cos\theta_B\ \sin\theta_B\ 0]^T \qquad \boldsymbol{n}_n = [-\sin\theta_B\ \cos\theta_B\ 0]^T \tag{60}$$

For the system under study, an exact computation should predict a zero tangential slip increment. The results obtained by replacing the previous equations into Eq.(36) can be thus interpreted as numerical errors if different from zero. Several approximations have been performed in these equations: e.g. the tangential vectors $\boldsymbol{t}_1$ and $\boldsymbol{t}_2$ and the normal vector $\boldsymbol{n}$ are evaluated at the previous time step.

The relative slip error $\epsilon_{slip} = g_{T2,n+1}/R$, defined as the incremental tangential slip divided by the distance between ball centers $R = r_A + r_B$, is obtained by replacing Eqs.(54–60) in Eq.(36), giving

$$\epsilon_{slip} = \sin(\theta_B)\left[1 - \cos(\theta_B) - \theta_B \sin(\theta_B)\right] + \cos(\theta_B)\left[\sin(\theta_B) - \theta_B \cos(\theta_B)\right] \tag{61}$$

Note that $\lim_{\theta_B \to 0} \epsilon_{slip} = 0$. Then, since $\theta_B \to 0$ when $(r_B/r_A) \to \infty$, Eq. (61) is exact when the radius r_B of the fixed sphere tends to ∞. A Taylor expansion around $\theta_B = 0$ of Eq.(61) gives

$$\epsilon_{slip} = -\frac{\theta_B^3}{6} + O(\theta_B^5) \tag{62}$$

Figure 28 shows a plot of the relative slip error as a function of ϕ_A for three different ratios (r_B/r_A) in a log-log scale. A third order convergence is observed.

Finally, Fig. 29 shows a plot of the relative slip error calculated as a function of the radius ratio (r_B/r_A), for three different values of ϕ_A. We remark from this figure that in order to gain accuracy, we should select A and B such that $r_B > r_A$.

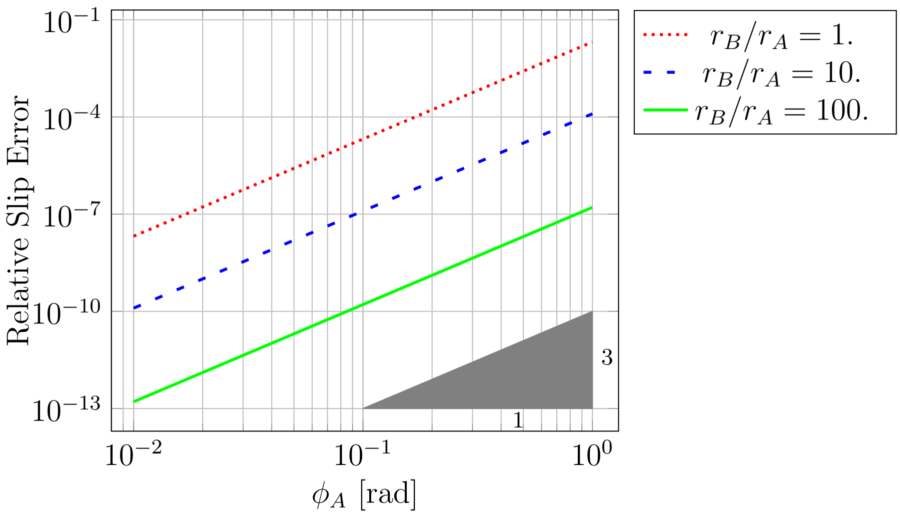

Figure 28: Relative slip error ϵ_{slip} as a function of the total angular displacement ϕ_A.

Appendix C

The following expressions are used for the example presented in Sec. 5.2 and can be found in [7]. The cue velocities after impact are given by the following expressions

$$\begin{aligned}
\omega_x^+ &= \frac{v^-}{R}\left[\frac{5}{4}\mu_b(1+e)\cos^3(\phi) - 1\right] \qquad \omega_y^+ = \frac{v^-}{R}\left[\frac{5}{4}\mu_b(1+e)\sin(\phi)\cos^2(\phi)\right] \\
v_x^+ &= \frac{v^-}{2}\sin(\phi)\cos(\phi)\left[1 + e - \mu_b(1+e)\cos(\phi)\right] \\
v_y^+ &= \frac{v^-}{2}\left[\sin^2(\phi)(2 - \mu_b(1+e)\cos(\phi)) + (1-e)\cos^2(\phi)\right]
\end{aligned} \tag{63}$$

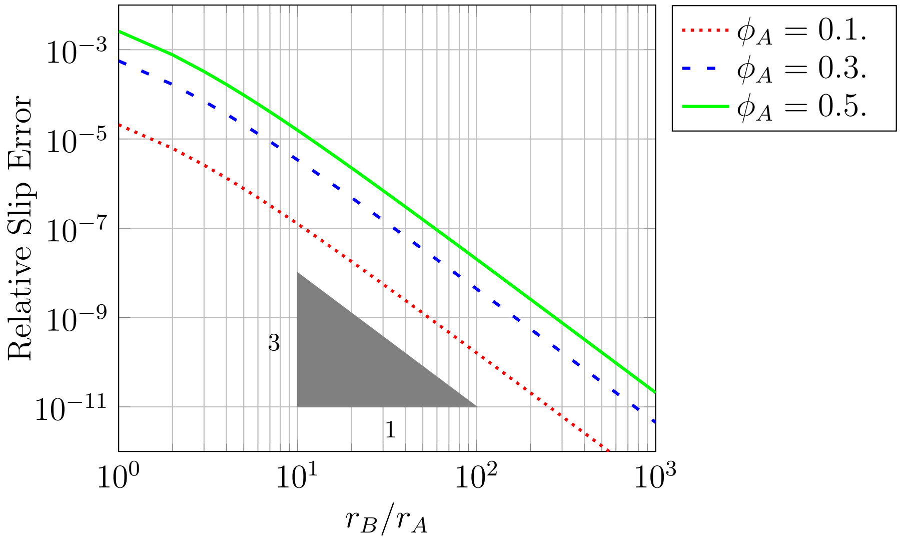

Figure 29: Relative slip error ϵ_{slip} as a function of the ratio r_B/r_A.

The velocity of the contact point between the cue ball and the table cloth immediately after cue ball impact with the objective ball is

$$v_{cx}^+ = v_x^+ - R\omega_y^+ \qquad v_{cy}^+ = v_y^+ - R\omega_x^+ \qquad v_c^+ = \sqrt{v_{cx}^2 + v_{cy}^2} \tag{64}$$

The time required for the cue ball to begin rolling is

$$t_{roll} = \frac{2v_c}{7\mu g} \tag{65}$$

The final cue ball velocity components are

$$v_{fx} = \frac{1}{7}\left(5v_x^+ + 2R\omega_y^+\right) \qquad v_{fy} = \frac{1}{7}\left(5v_y^+ - 2R\omega_x^+\right) \tag{66}$$

The position of the cue ball during the curved trajectory is

$$x_c(t) = v_x^+\ t - \frac{\mu\ g\ v_{cx}^+}{2v_c^+}t^2 \qquad y_c(t) = v_y^+\ t - \frac{\mu\ g\ v_{cy}^+}{2v_c^+}t^2 \tag{67}$$